# SPECTRAL TUNING OF LIQUID MICRODROPLETS STANDING ON A SUPERHYDROPHOBIC SURFACE BY USING A FOCUSED INFRARED LASER OR ELECTROWETTING

by

Yasin Karadağ

A Thesis Submitted to the
Graduate School of Engineering
in Partial Fulfillment of the Requirements for
the Degree of

Master of Science

in

Physics

Koç University

August, 2009

Koç University

Graduate School of Sciences and Engineering

This is to certify that I have examined this copy of a master's thesis by

Yasin Karadağ

and have found that it is complete and satisfactory in all respects,
and that any and all revisions required by the final
examining committee have been made.

Committee Members:

Alper Kiraz, Ph. D.(Advisor)

Adem Levent Demirel, Ph. D.

Metin Muradoğlu, Ph. D.

Date: _____

## ABSTRACT

Optical microcavities provide confinement of light into small volumes. They are favorable systems to use both for theoretical and experimental research areas. They are widely used in cavity quantum electrodynamics (CQED), optoelectronic, and biological sensing. Different types of optical microcavities have been demonstrated. Some types of them are fabry-perot resonators, microspheres, microdroplets, microtoroids.

Liquid microdroplets standing on a superhydrophobic surface can also provide a three dimensional confinement for light. The use of superhydrophobic surfaces is very efficient and costless way to protect the sphericity and provide the position stabilization of liquid microdroplets. The whispering gallery modes (WGMs) of liquid microdroplets can have high quality factors due to the large contact angle. The liquid nature of the microdroplets provides large spectral tuning which can not be obtained by using solid microcavities. The large spectral tuning of WGMs of liquid microdroplets can be obtained by the size change by using evaporation/condensation kinetics or the shape deformation by using electrowetting. In this thesis, first we demonstrate the large spectral tuning of a water-glycerol microdroplet standing on a superhydrophobic surface by local heating experimentally by optical spectroscopy and computationally using a lumped system formulation of the mass and heat transfer between the microdroplet and the chamber. The water-glycerol system is not fully reversible mainly due to glycerol content of the microdroplet. Some hysteresis effects due to whispering-gallery mode resonances are also observed in this system. Second, we obtain a fully reversible spectral tuning by using a highly soluble and nonvolatile inorganic salt instead of the glycerol content of the microdroplet. The self-stability and optical bistability are observed using NaCl-water microdroplet standing on superhydrophobic surface. Finally, we demonstrate reversible spectral tuning of the whispering gallery modes of glycerol-water microdroplets using electrowetting. We are able to obtain 4.7 nm spectral tuning at 400 V.

The techniques for large spectral tuning can inspire novel largely tunable microdroplet-based components required for optical communications systems. They can be used in cavity

quantum electrodynamics, and in characterizing liquid aerosols on surface. Also the spectral tuning with electrowetting can be used in measuring the contact angles of microdroplets standing on superhydrophobic surface. The self-stability of liquid microdroplets can provide stable experimental conditions for ultrahigh resolution spectroscopy of microdroplets. Optical bistability observed in photothermal tuning cycle can be used as a microdroplet-based optical memory device.

# ÖZETÇE

Optik mikrokovuklar ışığın küçük hacimler içinde hapsolmasını sağlar. Optik mikrokovuklar teorik ve deneysel araştırmalarda kullanılmak için tercih edilen sistemlerdir. Boşluk kuantum elektrodinamiğinde, optoelektonik alanında ve biyolojik algılamada sıklıkla kullanılırlar. Değişik tiplerde optik mikrokovuk şekilleri gösterilmişdir. Fabry-Perot çınlaçları, mikroküreler, mikrodamlacıklar ve mikrotoroidler bu tiplerin bazılarıdır.

Su tutmayan yüzey üzerinde duran sıvı mikrodamlacıklar ışık için üç boyutlu bir sınırlama sağlıyabilirler. Mikrodamlacık küreselliğinin korunması ve pozisyonunun sabitlenmesi için su tutmayan yüzeylerin kullanılması çok etkin ve maliyeti az bir yöntemdir. Yüksek kontak açılarına bağlı olarak sıvı damlacıkların fısıldayan galeri kipleri (FGKler) yüksek kalite faktörlerine sahip olurlar. Mikrodamlacıkların sıvı doğası, katı mikrokovuklar kullanılarak elde edilemeyen yüksek spektral taranmasına imkan verir. Elektoıslatma kullanılarak şekil deformasyonu ve buharlaşma-yoğunlaşma kinetiği kullanılarak boyut değiştirmesi ile mikrodamlacıkların fısıldayan galeri kiplerinin geniş spektral taranması elde edilebilir. Bu tezde ilk olarak su tutmayan yüzey üzerinde duran gliserol-su mikrodamlacıklarının geniş spektral taranması odaklanmış kızılötesi lazer kullanarak bölgesel ısıtma ile deneysel ve odacık ile mikrodamlacık arasındaki kütle ve ısı transferini formüle eden birleştirilmiş model kullanılarak sayısal olarak gösterildi. Mikrodamlacık içindeki gliserol nedeniyle su-gliserol sistemi tamamen ters çevrilebilir değildir. Fısıldayan galeri kiplerinin çınlanımına bağlı olarak bazı histerezis etkileri görüldü. İkinci olarak, mikrodamlacık içindeki gliserolün yerine buharlaşmayan ve suda çok fazla çözünebilen inorganik tuz kullanılarak tam olarak geri dönebilen spektral taranma elde edildi. Su tutamayan yüzey üzerinde duran NaCl-su damlacıkları kullanılarak özsabitleme ve optik iki durumluluk gösterildi. Son olarak olarak elektroıslatma kullanılarak su tutmayan yüzel üzerinde duran gliserol-su mikrodamlacıklarının fısıldayan galeri kiplerinin spekral taranması gösterildi. 400 V'ta 4.7 nm lik spekral taranma elde edildi.

Geniş spektral taranma için kullanılan teknikler optik iletişim sistemleri için gerekli olan

geniş ayarlanabilen mikrodamlacık temelli bileşenlere esin kaynağı olabilir. Bu teknikler yüzey üzerinde duran aerosolların karakterizasyonunda, boşluk kuantum elektrodinamiğinde kullanılabilir. Ayrıca, elekroıslatma ile spektral taranma su tutmayan yüzey üzerinde duran mikrodamlacıkların kontak açılarını ölçmek için kullanılabilir. Sıvı mikrodamlacıkların öz-sabitlemesi, ultra yüksek çözünürlükte mikrodamlacık spekroskopisi için sabit deneysel şartları sağlar. Işıklaısıtma ile tarama yapılırken gözlemlenen optik iki durumluluk mikrodamlacık temelli optik hafıza araçları olarak kullanılabilir.

## ACKNOWLEDGMENTS

First and foremost, I would like to thank my academic advisor, Asst. Prof. Alper Kiraz, for the guidance and support throughout my research topics. He is a great source of inspiration and patience. His scientific intuition and comprehension have always been very helpful.

I would like to thank Prof.Dr. Adem Levent Demirel and Assoc. Prof. Metin Muradoğlu for their support and advices in my thesis. It was my pleasure to collaborate with them, and they provided me great insights into different areas.

I am also grateful to Michael Mestre. I have greatly profited from the experimental and computational skills that he have taught me. It was a pleasure to work with him.

I would like to thank my colleagues Saime Çiğdem Yorulmaz, Mustafa Yorulmaz and Mustafa Gündoğan in Nano-Optics Research Laboratory.

Additionally, I also want to thank Ali Baş, Semih Afyon, Emre Yüce and M. S. Murib for their endless encouragement.

## TABLE OF CONTENTS

## LIST OF FIGURES

## NOMENCLATURE

| | |
|---|---|
| $a$ | microdroplet radius |
| $x_A$ | mole fraction of water |
| $x_B = (1 - x_A)$ | mole fraction of glycerol |
| $V_A$ | molar volume of water |
| $V_B$ | molar volume of glycerol |
| $V_m = x_A V_A + x_B V_B$ | molar volume of the microdroplet |
| $R$ | gas constant |
| $\Delta H_{vap,A}$ | latent heat of vaporization of water |
| $\Delta H_{vap,B}$ | latent heat of vaporization of glycerol |
| $C_{PA}$ | molar heat capacity of water |
| $C_{PB}$ | molar heat capacity of glycerol |
| $C_{PL} = x_A C_{PA} + x_B C_{PB}$ | molar heat capacity of the microdroplet |
| $D_A$ | gas phase diffusion coefficient of water in air |
| $D_B$ | gas phase diffusion coefficient of glycerol in air |
| $k_a$ | thermal conductivity of air |
| $k_s$ | thermal conductivity of the substrate |
| $T_d$ | microdroplet temperature |
| $T_\infty$ | temperature of air in the chamber |
| $P_A^0(T)$ | vapor pressure of water at temperature $T$ |
| $P_B^0(T)$ | vapor pressure of glycerol at temperature $T$ |
| $S_A$ | saturation ratio of water in air |
| $S_B$ | saturation ratio of glycerol in air |
| $N_A$ | number of moles of water in the microdroplet |
| $N_B$ | number of moles of glycerol in the microdroplet |
| $N = x_A N_A + x_B N_B$ | total number of moles in the microdroplet |
| $n_A$ | refractive index of water at 1064 nm |
| $n_B$ | refractive index of glycerol at 1064 nm |

# Chapter 1

# INTRODUCTION

## *1.1 Overview*

Spatial and temporal confinement of light is possible with optical microcavities. Mode volume (V) and quality factor (Q) are used to describe the spatial and temporal confinement, respectively. Mode volume is dependent on the energy density of the optical mode. The storage time of photon inside a resonator is determined by the quality factor. The light is confined inside the spherical cavity by total internal reflection. These modes are called whispering gallery modes (WGM).

Optical microcavities are favorable systems to use both for theoretical and experimental research fields. They are widely investigated in cavity quantum electrodynamics (CQED), optoelectronic, and biological sensing [1]. Different types of optical microcavities have been demonstrated. Some types of them are fabry-perot resonators [2], microspheres [3], microdroplets [4], microtoroids [5].

The existence of the atom inside the cavity can stop transmission if the probe frequency is the same as with the fundamental resonant frequency of the cavity [6]. Sensitive transmission due to the position of the atom inside the cavity can be used to determine atomic center-of mass motion [7, 8, 9]. Also dispersive properties have been observed from a cavity containing cold atoms [10].

High speed optical communication systems require dynamic filters and switches. A microcavity filter have been used to obtain resonant transfer between two waveguides [1]. The simplest form of this device is composed of a single whispering gallery microresonator inserted between two single-mode waveguides. This filter can serve as an active or passive filter. If it is used as a passive filter, a channel will dropped from the first waveguide with high extinction then it will couple to the second waveguide with low loss. The small size

of microcavity provides to use on a wafer [11]. If the refractive index is controlled, then the filter will be an active filter that will provide controllable resonant wavelength. Tuning [12], ultrafast modulation [13] and switching are possible with the controllable resonant wavelength.

Optical biosensors have become important tools in medicine and drug discovery [14]. High sensitivity is crucial for an optical biosensor. The optical resonances which are generated by the light confined in dielectric by total internal reflection are very sensitive. When the light get close to the surface of the microcavity, the sensitivity will increase. Adding a dielectric material to the microcavity surface causes the shifts of the optical resonances. By using these frequency shifts, the detection of biological molecules can be realized.

The problem with the solid microcavities is the solid nature which prevents the large tunability. In contrast to rigidity of solid microcavities, liquid microdroplets can be tuned easily due to their liquid nature. Using an electrodynamic trap or optical tweezer the position stabilization of liquid microdroplets is possible to conserve the sphericity. In addition these complex stabilization techniques, using superhydrophobic surface is very efficient and easy way to obtain large contact angles.

### *1.2 Thesis Outline*

The lumped system formulation of the mass and heat transfer between the microdroplet and the chamber and the calculation of normalized absorption efficiency according to the Lorentz-Mie Theory are explained in **Chapter 1**

In **Chapter 2**, large spectral tuning of water-glycerol microdroplet standing on a superhydrophobic surface by local heating with a focused infrared laser was demonstrated both experimentally and computationally.

In **Chapter 3**, a fully reversible spectral tuning of NaCl-water microdroplet, a self-stabilization mechanism locking the size of NaCl-water microdroplet standing on superhydrophobic surface and optical bistability between locked and unlocked states were demonstrated. The self-stabilization was resilient to the fluctuations in the ambient atmosphere. Also computational self-stability was shown in this chapter.

In **Chapter 4**, a reversible spectral tuning of the whispering gallery modes of a glycerol-water microdroplets standing on a superhydrophobic surface was demonstrated using elec-

trowetting. Maximum 4.7 nm spectral tuning was oberved at 400 V.

### *1.3 Superhydrophobic Surface Preparation*

Superhydrophobic surfaces were prepared by spin coating 50 mg/ml ethanol dispersion of hydrophobically-coated silica nanoparticles (Evonik, Aeroxide® LE1) on cover glasses [4, 15]. After spin-coating, the superhydrophobically coated-cover glasses were waited in an oven at 85℃, for one hour, for evaporation of the remaining ethanol after spin-coating. The diameter size of hydrophobic silica nanoparticles was between 7 nm and 20 nm. The superhydrophobic surfaces were transparent to visible light. The measured average contact angle of millimeter-sized droplets was larger than 155° on these surfaces. The average contact angle of micrometer-sized microdroplets is expected to be $1-2°$ smaller than that of millimeter sized droplets owing to Gibbs contact line tension [4, 16].

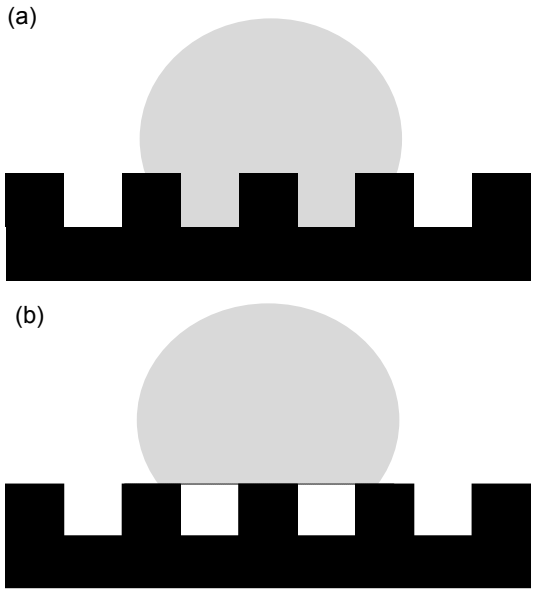


Figure 1.1: (a) Wenzel state, (b) Cassie-Baxter state

If a droplet is placed on a surface with roughness, the roughness structures on the surface can be filled by the droplet as shown in Fig.1.1a. This is called Wenzel state. Apart from Wenzel state, because of the capillary forces of the liquid, the droplet can not penetrate the roughness structures as shown in Fig.1.1b. The state is called as Cassie-Baxter state.

Hydrophobic surfaces that have the Cassie-Baxter and Wenzel state are called *slippy* or *sticky* surfaces, respectively [17].

### *1.4 Experimental Setup and Microdroplet Generation*

An ultrasonic nebulizer was used to generate water-glycerol microdroplets on the superhydropobic surface at room temperature. The volume ratio of water to glycerol was 90:10. Additionally, the solution contained 5 $\mu$M Rhodamine B. The diameter range of the microdroplets was between $8 - 20$ $\mu$m. As a result of water evaporation the microdroplet size decreases rapidly. The superhydrophobically coated cover glasses is taped under the humidity chamber. The relative water humidity of the chamber is stable and have a constant value. The stable humidity is provided by using saturated water solutions of different salts. The salts that are used in the experiments are $NaCl$, $KCl$, and $K_2SO_4$. When the saturated water solutions of $NaCl$,$KCl$, and $K_2SO_4$ are placed in the chamber, the relative water humidity of the chamber is 0.7530, 0.8434, and 0.9730 for $NaCl$, $KCl$, and $K_2SO_4$, respectively. The experimental setup is illustrated in Fig. 1.2.

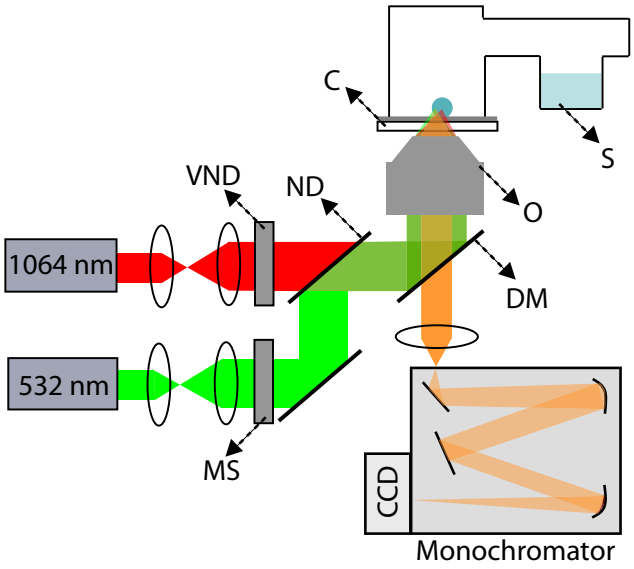


Figure 1.2: Illustration of the experimental setup. VND, variable neutral density filter; ND, neutral density filter; MS, mechanical shutter; DM, dichroic mirror; O, microscope objective; C, cover glass; SH, superhydrophobic coating; ST, saturated salt/water solution. A cw infrared solid state laser was used for local heating and a cw green solid state laser used for the excitation of the Rhodamine B molecules. The microdroplet is on the cover glass coated with hydrophobically coated silica nanoparticles.

Two continuous wave solid-state lasers are used. The infrared laser ($\lambda = 1064$ nm, maximum output power: $\sim 1$ W) is used for the local heating and the green laser ($\lambda =$

532 nm) is used to excite Rhodamine B molecules in the the microdroplet. A 2x telescope and 6x telescope are used to increase the beam size of the infrared laser and the green laser, respectively. The power of the infrared laser is adjusted by using a variable neutral density filter. Another neutral density filter is used to combine the beams of the infrared laser and the green laser. The combined beam is reflected by a dichroic mirror. The infrared laser and the green laser are focused to the center of the microdroplets and near the rim of the microdroplets using a high numerical microscope objective (NA=1.4 oil, 60x), in the inverted geometry. The rhodamine B emission due to excitation by the green laser is recorded to observe the WGMs. The Rhodamine B emission is transmitted through the dichroic mirror. Its beam size is magnified by using a 1.5x magnification element. It comes to a 50 cm monochromator (600 grooves/mm grating). The detection is done with a CCD camera and the exposure time is 0.5 sec. The mechanical shutter is open only during the exposure time. The spectral resolution of the experimental setup is 0.17 nm. The excitation powers of the infrared laser and the green laser at the focus of the microscope objective are $0-5$ mW and $\sim 1$ $\mu$W , respectively.

### *1.5 Whispering Gallery Modes*

Resonance modes are usually referred to as morphology-dependent resonances (MDRs), whispering-gallery modes (WGMs) and quasi-normal modes (QNMs). Optical properties of microspheres are related with the electromagnetic modes of the cavity. Suitable boundary conditions are satisfied by some resonance frequencies. At these frequencies the electric field is confined notably in the cavity. The difference between the modes of Fabry-Perot cavities and the modes of microspheres is the number of dimensions of confinement. The mode confinement direction of microspheres and Fabry-Perot cavities is three and one, respectively.

Total internal reflection occurs if the angle of incidence ($\theta_{inc}$) of the light propagating within a sphere of radius a is greater or equal than the critical angle ($\theta_c$).

$$\theta_{inc} \geq \theta_c = arcsin(1/\mathbf{m}(\omega)), \tag{1.1}$$

where $\mathbf{m}(\omega)$ is the index of refraction of the sphere.

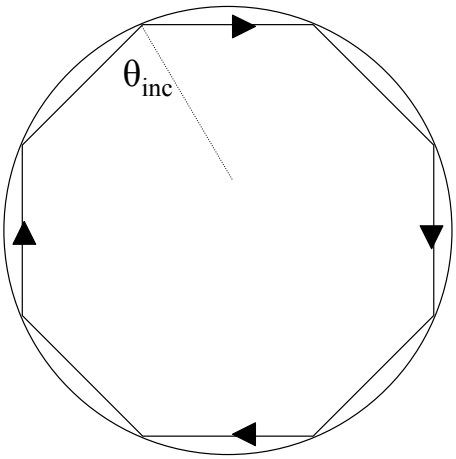


Figure 1.3: The ray at glancing angle is fully reflected. When the optical path is equal to the number of wavelengths, a resonance is formed.

Using the dimensionless size parameter $x = 2\pi a/\lambda$, the resonance condition for an internal ray is obtained as:

$$n = \mathbf{m}(\omega)x. \tag{1.2}$$

If the rays are not confined to the $x-y$ plane, the z-component of the angular momentum of the mode is

$$m = ncos(\theta). \tag{1.3}$$

All of the modes are degenerate (with $2n + 1$) for a perfect sphere. If the sphericity of the cavity deforms asymmetrically, the degeneracy is lifted. When there is a distortion like this, the integer values for $m$ are ±n,±(n-1)...0, where ± degeneracy rests since the resonance modes are independent of the circulation direction (clockwise or counterclockwise). A splitting occurs in the circulation $m$-mode frequencies due to two counter propagating modes [18]

The electric field can be expressed in terms of TE modes and TM modes. For TE modes, there is no radial component of the electric field and fo TM modes, there is no radial component of the magnetic field. The expressions for TE and TM modes are defined by

$$E_{TE} = z_n(\mathbf{m}(\omega)kr)X_{nm}(\theta, \phi), \tag{1.4}$$

$$E_{TM} = \nabla \times \{z_n(\mathbf{m}(\omega)kr)X_{nm}(\theta,\phi)\} \tag{1.5}$$

where $k$ is wave vector in free space, $z_n(\mathbf{m}(\omega)kr)$ is the spherical Bessel function for incident fields and internal fields that characterize the radial dependence of the fields, $z_n(\mathbf{m}(\omega)kr)$ is the spherical Hankel function for external fields. $\mathbf{m}(\omega)$ is the refractive index of the surrounding medium for incident fields, the refractive index of the sphere for the internal fields. $X_{nm}(\theta,\phi)$ is the vector spherical harmonics that characterizes the angular distribution of the electric fields and described by

$$X_{nm}(\theta,\phi) = \frac{-i}{\sqrt{n(n+1)}} r \times \nabla Y_{nm}(\theta,\phi), \tag{1.6}$$

where $Y_{nm}(\theta,\phi)$ are the spherical harmonics. By matching the tangentinal components of $\mathbf{E}$ and $\mathbf{H}$ at the boundary, the chracteristic equation is obtained. The characterestic equation of a sphere of radius $a$ and index of refraction $\mathbf{m}(\omega) = \mathbf{m}_r(\omega) + i\mathbf{m}_i(\omega)$ in air for TM resonances defined by

$$\frac{\psi_n'(\mathbf{m}(\omega)x)}{\psi_n(\mathbf{m}(\omega)x)} - \mathbf{m}(\omega)\frac{\zeta_n'(x)}{\zeta_n(x)} = 0. \tag{1.7}$$

The characteristic equation for TE resonances is

$$\mathbf{m}(\omega)\frac{\psi_n'(\mathbf{m}(\omega)x)}{\psi_n(\mathbf{m}(\omega)x)} - \frac{\zeta_n'(x)}{\zeta_n(x)} = 0, \tag{1.8}$$

where $x = ka = 2\pi a/\lambda$ is the size parameter, $\psi_n$ is the Ricatti-Bessel function, $\zeta_n$ is the Ricatti-Henkel function. If there is no loss ($\mathbf{m}_i(\omega)$=0), the solutions to Eq.(1.7) and Eq.(1.8) are the complex resonance size parameters $x_\alpha$. The resonant frequencies for a fixed radius sphere are designated by the real part of the size parameters. The leakage loss of the mode out of the absorptionless dielectric cavity is related with the imaginary part of the size parameter.

There are several independent equations represented by Eq.(1.7) and Eq.(1.8) for each mode number $n$. The solutions of these transcendental equations correspond to the resonances, or MDRs. Also, the radial mode number $l$ is obtained from these solutions for each $n$. For a fixed $n$ and $\mathbf{m}(\omega)$, the first and second solutions are labeled $l$=1 and $l$=2, respectively. The physical interpretation is that the number of intensity maxima of the

mode along $r = a/\mathbf{m}(\omega)$ to $r = a$ is $l$. The resonance size parameters of a perfect sphere are independent of $m$. The resonance modes are generally represented by their polarization $TM_{n,l}$ and $TE_{n,l}$. The relation between the real part of $x_\alpha$ and the resonance frequency is

$$\omega_\alpha = cRe(x_\alpha)/a. \tag{1.9}$$

The FWHM of the MDR is twice the imaginary part of $x_\alpha$. The FWHM of the mode is denoted $\nabla x_\alpha$ or $\nabla \omega_\alpha$. The quality factor ($Q$) of the resonance is represented as

$$Q = \frac{Re(x_\alpha)}{2Im(x_\alpha)} = \frac{\omega_\alpha}{\nabla \omega_\alpha} = \omega_\alpha \tau, \tag{1.10}$$

where $\tau$ is the wave lifetime on the resonance. Diffractive leakage losses limit the $Q$ values. The maximum $Q$ can be as high as $10^{100}$ for a perfect lossless sphere. There are some factors like volume inhomogeneities, surface roughness, shape deformations, nonlinear effects and absorption that limits the maximum $Q$ values to be less than $10^{10}$ [19].

Chapter 2

# MODELLING PHOTOTHERMAL TUNING OF LIQUID MICRODROPLETS AND $\tilde{Q}_{ABS}$ CALCULATION

## *2.1 Introduction*

We defined a lumped equation model for the evaporation and growth of water-glycerol and NaCl-water microdroplets standing on a superhydrophobic surface due to local heating by a focused infrared laser. The generalized Lorenz-Mie theory [20, 21, 22] is used to calculate the absorption of the focused laser beam by the microdroplet.

## *2.2 Rate equation model for a water-glycerol microdroplet standing on a superhydrophobic surface*

The mass and heat transfer between the microdroplet and the chamber is simulated by using a lumped system model according to Ray et al. [23, 24]. This model assumes the uniform temperature and composition distributions within the microdroplet for all times. Also, the effect of the heat and mass transfer within the microdroplet is more than the heat and mass transfer across a microdroplet interface. The uniform temperature inside the microdroplet is a good approximation when the Biot number is much smaller than 1. In addition to that, the molecular diffusion in a quasi-stationary state makes the transition time sufficiently slow. Using these assumptions, the number of moles of component $A$ (water) $N_A$ and $B$ (glycerol) $N_B$ in the microdroplet of radius $a$ derived by

$$\frac{dN_A}{dt} = -4\pi a f_{PB} D_A \frac{P_A^0(T_\infty)}{RT_\infty} \left(\gamma_A x_A \phi_A - S_A\right), \tag{2.1}$$

$$\frac{dN_B}{dt} = -4\pi a f_{PB} D_B \frac{P_B^0(T_\infty)}{RT_\infty} \left(\gamma_B x_B \phi_B - S_B\right), \tag{2.2}$$

where

$$\phi_A = \left(\frac{T_\infty}{T_d}\right) \frac{P_A^0(T_d)}{P_A^0(T_\infty)}; \quad \phi_B = \left(\frac{T_\infty}{T_d}\right) \frac{P_B^0(T_d)}{P_B^0(T_\infty)}. \tag{2.3}$$

In Eqs.(2.1-2.3), the subscripts $A$ and $B$ denote properties of the components $A$ and $B$, respectively, $D_{A,B}$ is the molecular diffusivity in the gas mixture, $\gamma_{A,B}$ is the activity coefficient, $x_{A,B}$ is the mole fraction, $S_{A,B}$ is the relative humidity in the chamber, $R$ is the universal gas constant, $P^0_{A,B}(T)$ is the vapor pressure at temperature $T$, and $T_d$ and $T_\infty$ are the temperatures at the microdroplet interface and in the chamber far from the microdroplet, respectively. The effects of the substrate on the mass transfer is included to the equations and defined as the correction factor $f_{PB}$ given by Picknett and Bexon [25, 26] equation:

$$f_{PB}(\theta) = \frac{1}{2}\begin{cases} 0.6366\theta + 0.09591\theta^2 - 0.06144\theta^3 & 0^o \leq \theta < 10^o \\ 0.000008957 + 0.6333\theta + 0.116\theta^2 - 0.08878\theta^3 + 0.01033\theta^4 & 10^o \leq \theta < 180^o, \end{cases} \tag{2.4}$$

where $\theta$ is the contact angle. The contact angle for millimeter-size droplets standing on a superhydrophobic surface is obtained experimentally to be about $160^o$. The contact angle is not expected to be very different for micrometer-sized droplets standing on a superhydrophobic surface. The temperature change in the droplet evolves by:

$$\frac{dT_d}{dt} = \frac{\Delta H_{vap,A}}{NC_{PL}}\frac{dN_A}{dt} + \frac{\Delta H_{vap,B}}{NC_{PL}}\frac{dN_B}{dt} - \frac{3k_{\text{eff}}V_m}{a^2C_{PL}}(T_d - T_\infty) + \frac{\tilde{Q}_{abs}P_{inc}}{NC_{PL}}, \tag{2.5}$$

where $V_m$ is the molar specific volume, $N$ is the total number of moles, $C_{PL}$ is the molar heat capacity of the glycerol-water microdroplet, $\Delta H_{vap,A,B}$ is the enthalpy of evaporation and $k_{\text{eff}}$ is the effective heat conductivity. We defined $k_{\text{eff}}$ as the area average heat conductivities of air($k_a$) and substrate ($k_s$). $k_{\text{eff}}$ can be written as:

$$k_{\text{eff}} = f_a k_a A_a + (1 - f_a)k_s, \tag{2.6}$$

where $f_a$ can be defined as:

$$f_a = A_a/A_d. \tag{2.7}$$

In Eqn. (2.7) $A_a$ is the surface area of the microdroplet that is in contact with the air and $A_d$ is the total surface area of the microdroplet. $\tilde{Q}_{abs}$ in Eq. (2.5) defines the ratio of the total power absorbed by the microdroplet to the total power of the incident beam ($P_{inc}$). The activity coefficients of water and glycerol are calculated by Gibbs-Duhem and

**Table 2.1: Constants [27, 28]**

| Constant | Value | Unit |
|---|---|---|
| $V_A$ | $18.0153 \cdot 10^{-6}$ | $m^3/mol$ |
| $V_B$ | $73.03 \cdot 10^{-6}$ | $m^3/mol$ |
| $R$ | 8.314472 | $J/(mol \cdot K)$ |
| $\Delta H_{vap,A}$ | 40714.578 | $J/mol$ |
| $\Delta H_{vap,B}$ | 61000 | $J/mol$ |
| $C_{PA}$ | 75.327 | $J/(mol \cdot K)$ |
| $C_{PB}$ | 221.193 | $J/(mol \cdot K)$ |
| $D_A$ | $24.2 \cdot 10^{-6}$ | $m^2/sec$ |
| $D_B$ | $8.7710 \cdot 10^{-6}$ | $m^2/sec$ |
| $k_a$ | 0.02620 | $W/(m \cdot K)$ |
| $k_s$ | 1.14 | $W/(m \cdot K)$ |
| $n_A$ | $1.33 + 1202.32 \cdot 10^{-9}i$ | |
| $n_B$ | $1.47 + 1811.95 \cdot 10^{-9}i$ | |

van Laar equations, respectively. The van Laar equation for water activity coefficient($\gamma_A$) is:

$$\ln \gamma_A = \frac{c_1}{\left(1 + \frac{c_1}{c_2}\frac{x_A}{1-x_A}\right)^2}, \tag{2.8}$$

. Where the parameters $c_1 = -0.3049$ and $c_2 = -0.8551$. There values are determined by the best fit to the experimental data by Tu and Ray [24].

The Gibbs-Duhem equation for the glycerol activity coefficient($\gamma_B$)is:

$$\ln \gamma_B = \frac{c_2}{c_1}\left(2\sqrt{c_1 \ln \gamma_A} + \ln \gamma_A + c_1\right). \tag{2.9}$$

Fig. 2.1a shows the steady state situation between the microdroplet and the environment assuming that $T_\infty = 299.55\ K$ and glycerol is ideally nonvolatile. At the steady state $S_A$ equals to $\gamma_A x_A \phi_A$ and $T_d$ is larger than $T_\infty$. When $T_d$ increases, $x_A$ decreases. If we look at the fixed value of $S_A$ we can see that the change of $x_A$ is more prominent at high relative

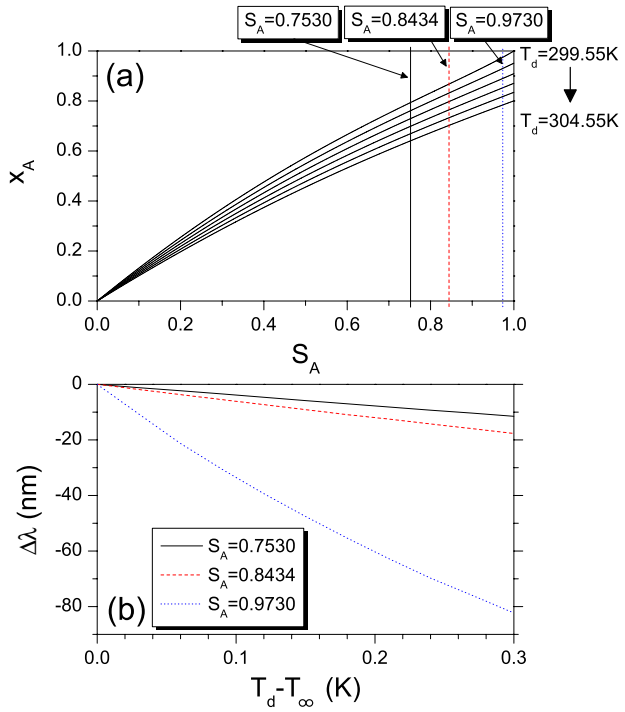


Figure 2.1: Steady state analysis assuming that glycerol is ideally nonvolatile. (a) Steady mole fraction of water as a function of relative humidity of water for various values of microdroplet temperature ($T_d$) assuming the temperature of the chamber ($T_\infty$) to be 299.55 K. Vertical lines indicate the relative humidities of water used in the experiments. (b) The spectral drift in the WGMs located at around 590 nm as a function of $T_d - T_\infty$.

water humidities. Hence at high relative water humidities ($S_A > 0.9$) the large size change of the droplet is possible with the small variation in droplet temperature. At high relative water humidities, there is very little amount of glycerol in the microdroplet. Due to high volatility of water than glycerol large tuning of microdroplet is obtained at high relative water humidities. For the center wavelength 590 nm, the spectral change of the WGMs as a function of $T_d - T_\infty$ is shown in Fig. 2.1b for three different $S_A$ values. The linear equation between the spectral position of the WGMs and the normalized equtorial radius is given as [29, 30]:

$$\frac{\Delta a}{a} = \frac{\Delta \lambda}{\lambda}, \tag{2.10}$$

.

### *2.3 Rate equation model for a NaCl-water microdroplet standing on a superhydrophobic surface*

In this case, water is the only volatile component in the droplet. The change in the number of moles of component $A$ (water) in the microdroplet of radius $a$ and the change in the temperature of the microdroplet in the time is the same as Eq.2.1 and Eq.2.5, respectively. By using the polynomial best fit given in ref.[31], the water activity coefficient ($\gamma_A$) and the solution density ($d$) are calculated as

$$\gamma_A = 1.0 + \sum C_i x_{WP}^i \tag{2.11}$$

$$d = 0.9971 + \sum A_i x_{WP}^i \tag{2.12}$$

where $C_1 = -6.366 \times 10^{-3}$, $C_2 = 8.624 \times 10^{-5}$, $C_3 = -1.158 \times 10^{-5}$, $C_4 = 1.518 \times 10^{-7}$, $A_1 = 7.41 \times 10^{-3}$, $A_2 = -3.741 \times 10^{-5}$, $A_3 = 2.252 \times 10^{-6}$, $A_4 = -2.06 \times 10^{-8}$, and $x_{WP}$ represents the solute weight percent.The real and imaginary parts of the refractive index were determined considering the concentration of salt in the microdroplet and the wavelength of the laser [31, 32, 33, 28].

### *2.4 Generalized Lorentz-Mie Theory*

Lorentz-Mie Theory can be insufficient when the size of the spherical particle is not small enough with respect to the beam diameters [34]. Generalized Lorentz-Mie Theory is required for these situations. There are three waves due to particle/laser interaction. These are the scattered wave outside the sphere, the sphere wave inside the sphere, and the incident wave. The main goal is to obtain solutions to these electromagnetic waves by using the boundary conditions at the surface of the sphere. The electromagnetic field components are [35, 36]

$$E_r = \frac{\partial^2 (r^e \Pi)}{\partial r^2} + k^2 r^e \Pi, \tag{2.13}$$

$$E_\theta = \frac{1}{r} \frac{\partial^2 (r^e \Pi)}{\partial \theta \partial r^2} + \frac{k''}{r sin\theta} \frac{\partial (r^m \Pi)}{\partial \Phi}, \tag{2.14}$$

$$E_\phi = \frac{1}{r sin\theta} \frac{\partial^2 (r^e \Pi)}{\partial \phi \partial r^2} - \frac{k''}{r} \frac{\partial (r^m \Pi)}{\partial \theta}, \tag{2.15}$$

$$H_r = \frac{\partial^2 (r^m \Pi)}{\partial r^2} + k^2 r^m \Pi, \tag{2.16}$$

$$H_\theta = -\frac{k^{'}}{r sin\theta} \frac{\partial (r^e \Pi)}{\partial \phi} + \frac{1}{r} \frac{\partial^2 (r^m \Pi)}{\partial r \partial \phi}, \tag{2.17}$$

$$H_\phi = -\frac{k^{'}}{r} \frac{\partial (r^e \Pi)}{\partial \theta} + \frac{1}{r sin\theta} \frac{\partial^2 (r^m \Pi)}{\partial r \partial \phi}, \tag{2.18}$$

where ${}^e\Pi$ is the scalar potential associated with the electric field, ${}^m\Pi$ is the scalar potental associated with the magnetic field, $k^{'} = ik_0\bar{\epsilon}$, $k^{''} = ik_0\bar{\epsilon}$ and $k = k_0\sqrt{\bar{\epsilon}}$. The complex dielectric constant is $\bar{\epsilon} = \epsilon + i4\pi\sigma/\omega$. $\sigma$ is the electrical conductivity. ${}^e\Pi$ and ${}^m\Pi$ satisfy the Helmhotz equation

$$\nabla^2 \Pi + k^2 \Pi = 0. \tag{2.19}$$

The most general separation of variables solution of the Helmholtz equation (Eq.2.19) is

$$r\Pi = \sum_{l=0}^{\infty} \sum_{m=-l}^{l} \left[ \tilde{A}_{lm} \psi_l (kr) + \tilde{B}_{lm} \chi_l (kr) \right] Y_{lm}(\theta, \phi), \tag{2.20}$$

where $\tilde{A}_{lm}$, $\tilde{B}_{lm}$ are the arbitrary constants, $\psi_l$ and $\chi_l$ are the Ricatti-Bessel functions and $Y_{lm}(\theta, \phi)$ is the spherical harmonic function.

The wave scalar potentials of the electric and magnetic fields for the incident field (superscript i), the scattered field (superscript s) and the internal field (superscript w) are [35, 36]

$$r^e\Pi_{(i)} = \sum_{l=0}^{\infty} \sum_{m=-l}^{l} A_{lm} \psi_l (k_{ext} r) Y_{lm}(\theta, \phi), \tag{2.21}$$

$$r^m\Pi_{(i)} = \sum_{l=0}^{\infty} \sum_{m=-l}^{l} B_{lm} \psi_l (k_{ext} r) Y_{lm}(\theta, \phi), \tag{2.22}$$

$$r^e\Pi_{(s)} = \sum_{l=0}^{\infty} \sum_{m=-l}^{l} a_{lm} \xi_l^{(1)} (k_{ext} r) Y_{lm}(\theta, \phi), \tag{2.23}$$

$$r^m\Pi_{(s)} = \sum_{l=0}^{\infty} \sum_{m=-l}^{l} b_{lm} \xi_l^{(1)} (k_{ext} r) Y_{lm}(\theta, \phi), \tag{2.24}$$

$$r^e \Pi_{(w)} = \sum_{l=0}^{\infty} \sum_{m=-l}^{l} c_{lm} \xi_l^{(1)} \left(k_{ext} r\right) Y_{lm}(\theta, \phi), \tag{2.25}$$

$$r^m \Pi_{(w)} = \sum_{l=0}^{\infty} \sum_{m=-l}^{l} d_{lm} \xi_l^{(1)} \left(k_{ext} r\right) Y_{lm}(\theta, \phi), \tag{2.26}$$

where $\xi_l^{(1)} = \psi_l - i\chi_l$. $\chi_l$ have been ignored for the incident and the internal field because these functions are unbounded at the origin.

The incident, scattered and internal electromagnetic fields are provided by substituting Eqs. 2.21-2.26 into Eqs. 2.13-2.18. After finding the electric field and magnetic field components of the incident, scattering and internal electric fields, the coefficients that describe the fields can be find using appropriate boundary conditions. The tangential components of the electric and magnetic fields are continuous across the sphere surface.

The coefficients that describe the scattered field are defined as [37];

$$a_{lm} = \frac{\psi_l^{'}\left(k_{int}a\right)\psi\left(k_{ext}a\right) - \bar{n}\psi_l\left(k_{int}a\right)\psi_l^{'}\left(k_{ext}a\right)}{\bar{n}\psi_l\left(k_{int}a\right)\xi_l^{(1)'}\left(k_{ext}a\right) - \psi_l^{'}\left(k_{int}a\right)\xi_l^{(1)}\left(k_{ext}a\right)} A_{lm}, \tag{2.27}$$

$$b_{lm} = \frac{\bar{n}\psi_l^{'}\left(k_{int}a\right)\psi\left(k_{ext}a\right) - \psi_l\left(k_{int}a\right)\psi_l^{'}\left(k_{ext}a\right)}{\psi_l\left(k_{int}a\right)\xi_l^{(1)'}\left(k_{ext}a\right) - \bar{n}\psi_l^{'}\left(k_{int}a\right)\xi_l^{(1)}\left(k_{ext}a\right)} B_{lm}. \tag{2.28}$$

The coefficients that decribe the internal field are defined as [37];

$$c_{lm} = \frac{\xi_l^{(1)'}\left(k_{ext}a\right)\psi\left(k_{ext}a\right) - \xi_l^{(1)}\left(k_{ext}a\right)\psi_l^{'}\left(k_{ext}a\right)}{\bar{n}^2\psi_l\left(k_{int}a\right)\xi_l^{(1)'}\left(k_{ext}a\right) - \bar{n}\psi_l^{'}\left(k_{int}a\right)\xi_l^{(1)}\left(k_{ext}a\right)} A_{lm}, \tag{2.29}$$

$$d_{lm} = \frac{\xi_l^{(1)'}\left(k_{ext}a\right)\psi\left(k_{ext}a\right) - \xi_l^{(1)}\left(k_{ext}a\right)\psi_l^{'}\left(k_{ext}a\right)}{\psi_l\left(k_{int}a\right)\xi_l^{(1)'}\left(k_{ext}a\right) - \bar{n}\psi_l^{'}\left(k_{int}a\right)\xi_l^{(1)}\left(k_{ext}a\right)} B_{lm}. \tag{2.30}$$

The localized beam shape coefficients $A_{lm}$ and $B_{lm}$ that decribe the incident field are defined as [21];

$$A_{lm} = \begin{cases} A_{lm}^{+}, & \text{if } \ m > 0, \\ A_{lm}^{-}, & \text{if } \ m > 0, \\ A_{l0}, & \text{if } \ m = 0. \end{cases} \tag{2.31}$$

$$A_{lm}^{\pm} = F_l \left(\frac{-r_f^{\pm}}{l + \frac{1}{2}}\right)^{m-1} \left[J_{m-1}(P) - (r_f^{\pm})^2 J_{m+1}(P)\right]. \tag{2.32}$$

$$A_{l0}^{\pm} = F_l \frac{2l(l+1)}{l+\frac{1}{2}} \frac{x_f}{(x_f^2+y_f^2)^{1/2}} J_1(P), \tag{2.33}$$

with

$$r_f^{\pm} = \frac{x_f \pm y_f}{(x_f^2+y_f^2)^{1/2}}, \tag{2.34}$$

$$P = -\frac{l+\frac{1}{2}}{z_f/w_0} \left(\frac{x_f^2+y_f^2}{w_0^2}\right)^{1/2} \left(1+\frac{iw_0}{2sz_f}\right)^{-1}. \tag{2.35}$$

Similarly,

$$B_{lm} = \begin{cases} B_{lm}^{+}, & \text{if } \ m>0, \\ B_{lm}^{-}, & \text{if } \ m>0, \\ B_{l0}, & \text{if } \ m=0, \end{cases} \tag{2.36}$$

where

$$B_{lm}^{\pm} = \frac{\pm F_l}{i} \left(\frac{-r_f^{\pm}}{l+\frac{1}{2}}\right)^{m-1} \left[J_{m-1}(P) + (r_f^{\pm})^2 J_{m+1}(P)\right], \tag{2.37}$$

$$B_{l0}^{\pm} = F_l \frac{2l(l+1)}{l+\frac{1}{2}} \frac{y_f}{(x_f^2+y_f^2)^{1/2}} J_1(P), \tag{2.38}$$

In these equations $F_1$ defined as

$$F_1 = D\left[-D\left(\frac{x_f^2+y_f^2}{w_0^2}\right)\right] exp\left[-Ds^2\left(I+\frac{1}{2}\right)^2\right] \times exp\left(\frac{-i}{s}\frac{z_f}{w_0}\right) \tag{2.39}$$

where

$$s = \frac{1}{kw_0}, \tag{2.40}$$

$$D = \left(1-\frac{2isz_f}{w_0}\right)^{-1}. \tag{2.41}$$

The time-averaged power absorbed by the sphere can be defined by integrating the radial component of the external field Poynting vector over a surface enclosing the sphere. For the large integration radius, it is defined as [35, 36]

$$W_{abs} = -\frac{c}{8\pi} k_0^2 \epsilon_{ext} \sum_{m=-l}^{l} l\,(l+1)\left[|a_{lm}|^2 + |b_{lm}|^2 + Re\,(A_{lm}a_{lm}^* + B_{lm}b_{lm}^*)\right]. \tag{2.42}$$

The ratio of the total power absorbed by the sphere to the total power of the incident beam is defined as modified absorption efficiency ($\tilde{Q}_{abs}$). Using the value of the total power

of the incident beam is $(c/16)E_0^2 w_0^2$ where $E_0^2$ is the electric field amplitude at the beam focus, the modified absorption efficiency is defined as

$$\tilde{Q}_{abs} = -\frac{2\alpha_2}{\pi \tilde{w}_0^2 \alpha_4 E_0^2} \sum_{m=-l}^{l} l\,(l+1) \left[ |a_{lm}|^2 + |b_{lm}|^2 + Re\,(A_{lm} a_{lm}^* + B_{lm} b_{lm}^*) \right]. \qquad (2.43)$$

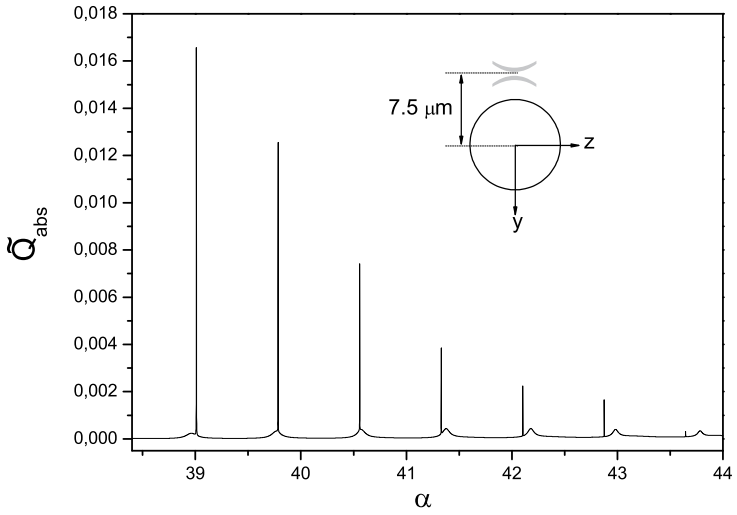


Figure 2.2: The modified absorption efficiency ($\tilde{Q}_{abs}$) as a function of the size parameter ($\alpha$). Calculations are made for a sphere suspended in air by using the localized approximation to the beam-shape coefficients in generalized Lorenz-Mie theory. The laser propagating in z and polarized in x directions is focused near the vicinity of the rim of the sphere at y=7.5 $\mu$m.

The calculation of $\tilde{Q}_{abs}$ as a function of the size parameter $\alpha = 2\pi a/\lambda$, for a 7 $\mu$m spherical particle suspended in air is shown in Fig.2.2. Only first order TE modes are excited due to off-axis excitation [21].

Chapter 3

# WATER-GLYCEROL MICRODROPLET STANDING ON A SUPERHYDROPHOBIC SURFACE

## *3.1 Introduction*

We examined the characterization and modeling of the spectral tuning of water-glycerol microdroplets standing on a superhydrophobic surface which were heated locally by a focused infrared laser. When a water-glycerol microdroplet is heated, its temperature becomes higher than the the temperature of the humidity chamber. The amount of water in the microdroplet decreases due to evaporation, then the size decreases and reaches an equilibrium with the surrounding. When the infrared laser is switched off closed, the temperature of the microdroplet decreases. The amount of water in microdroplet increases due to water adsorption. The size increases until a new thermodynamic equilibrium is reached with the surrounding. If there is enough glycerol in the chamber, the initial and final size of the microdroplet will be nearly the same. In addition to glycerol in the chamber, the reversibility of the photothermal tuning is dependent on the relative water humidity of the chamber.

*Negligible Deformation Due to the Optical Scattering Force*

The optical scattering force can cause size deformation. This deformation is negligible since it is smaller than the spectral tuning caused by the local heating. Due to the spectral resolution of the experimental setup, this deformation caused by the optical scattering force can not be detected.

If the scattering force $F_{scat}$ is in the upward direction, the horizontal radius $r_h$ of the microdroplet decreases and the vertical radius $r_v$ increases. Consequently, the spherical microdroplet becomes as a prolate spheroid as shown in Fig. 3.1. According to equilibrium condition, $F_{scat}$ is given by

$$F_{scat} = 2\pi r_h \sigma_{lv} - \pi r_h^2 \Delta P, \tag{3.1}$$

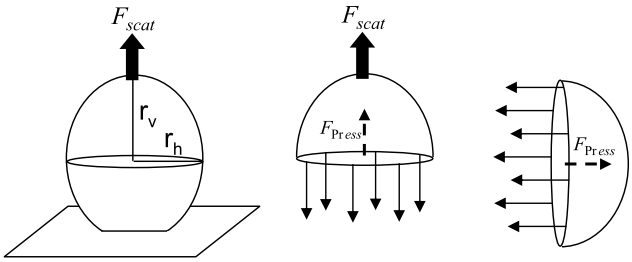


Figure 3.1: Illustrations of deformation caused by the optical scattering scattering force (left) and force balance in vertical (middle) and horizontal (right) directions.

where $\sigma_{lv}$ is the surface tension. $\Delta P$ is the pressure difference between outside and inside of the microdroplet and is called the Laplace pressure. The force balance in the horizontal direction can be written as

$$\pi r_v^2 \Delta P = 2\pi r_v \sigma_{lv}, \tag{3.2}$$

$$\Delta P = \frac{2\sigma_{lv}}{r_v}. \tag{3.3}$$

Using this result in Eq. 3.1 yields

$$F_{scat} = 2\pi r_h \sigma_{lv} \left(1 - \frac{r_h}{r_v}\right). \tag{3.4}$$

For a water-glycerol microdroplet, $r_h$ is between $3.3 - 4.5$ $\mu$m. The value of the surface tension for a water-glycerol microdroplet is between the surface tension of water ($72 \cdot 10^{-3}$ N/m) and the surface tension of glycerol ($63 \cdot 10^{-3}$ N/m). According to the method which was explained by Ref. [38], the scattering force is calculated for a microdroplet which is excited by a focused infrared laser. We find that $F_{scat}$ is approximately 1-2 pN due to 5 mW incident laser power. The spectral shift is defined as,

$$\Delta\lambda = \lambda \frac{\Delta r_h}{r_h} \tag{3.5}$$

where $\lambda$ is the spectral position of the whispering gallery modes(WGMs) [29, 30]. For a 4 $\mu$m radius water-glycerol microdroplet the spectral shift is between 0.0004-0.0008 nm which is much smaller than the spectral resolution of our experimental setup (0.17 nm). Therefore, the optical scattering force can not be a reason for the observed large spectral tuning.

*Laser-induced heating*

The generalized Lorentz-Mie theory is used to compute the laser-induced heating of a spherical microdroplet suspended in air due to a focused infrared laser [20, 21]. Fig.3.2 shows the normalized absorption efficiency ($\tilde{Q}_{abs}$) as a function of the structure factor ($\alpha$) for three relative water humidities used in the experiments. The wavelength ($\lambda$) and focal waist ($w_0$) value used in the calculations are 1064 nm and 1000 nm, respectively. According to the Ref. [27], the refractive index of the microdroplet is calculated as $n_L = v_A n_A + v_B n_B$, where $v_A$ and $v_B$ denote the volume fractions of water and glycerol, respectively. The complex refractive indices of water and glycerol are taken as $n_A = 1.33 + 1202.32 \cdot 10^{-9} i$ and $n_B = 1.47 + 1811.95 \cdot 10^{-9} i$ [33]. In Fig.3.2, the high quality WGMs are not observed owing to the on-axis illumination. The low quality modes are the Fabry-Perot resonance modes [37]. For $\alpha > 50$, the normalized absorption efficiency of the microdroplet exactly matches with the absorption of a dielectric slab with a thickness of $2a$. In our experiments, the microdroplets are standing on superhydrophobic surfaces that is a reason of an error in the ($\tilde{Q}_{abs}$). If we think of a simple model that consists of three dielectric layers (glass/microdroplet/air), 5% more laser induced heating is required due to the omission of the substrate.

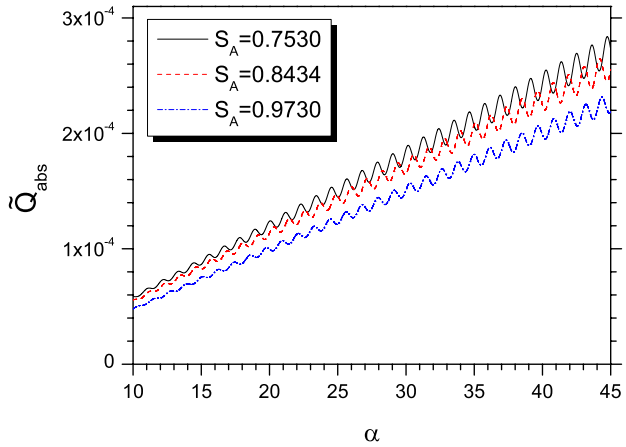


Figure 3.2: Normalized absorption efficiency as a function of the structure factor ($\alpha = 2\pi a/\lambda$) for the three different relative water humidities used in the experiments. A perfectly spherical microdroplet is assumed to be suspended in air, and the effects of the superhyrophobic substrate are ignored. Low quality oscillations are due to the Fabry-Perot resonance modes.

### *3.2 Experimental and Computational Results*

The spectral drift of a 7.6 $\mu$m diameter microdroplet is shown on Fig. 3.3. KCI solution is used as a calibration salt solution. It provides relative water humidity of 0.8434 in the chamber. Firstly, the infrared laser power is increased gradually. The infrared laser power range is between 0 and 3.9 mW. Due to the decrease in size, a blue shift of the WGMs is observed. Then the laser power is decreased gradually to zero. A red shift of the WGMs is observed. Arrows show the spectral drift of the high quality WGM A during the local heating. The maximum spectral drift is 11.5 nm at the maximum infrared laser power. There is a blue shift (1.2 nm) between the initial and final spectral positions of the WGM A at the end of the experiment. This blue-shift is attributed to the evaporation of glycerol. The unchanging lineshape function of the WGM shows that the sphericity and the contact angle are well preserved during the spectral tuning.

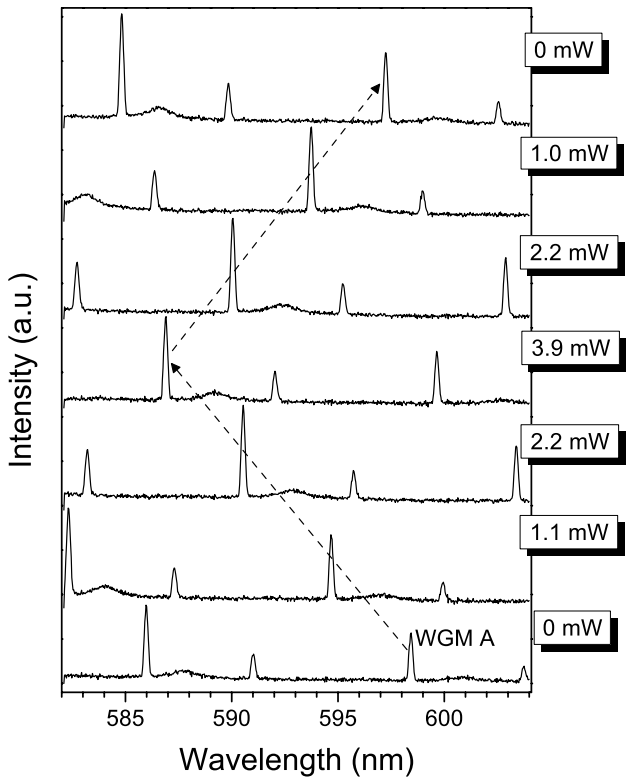


Figure 3.3: Emission spectra recorded from a 7.6 $\mu$m diameter microdroplet while the infrared laser power is first increased from and then decreased to zero. Arrows indicate the spectral drift direction of the high quality WGMs belonging on the same mode set. At the maximum infrared laser power of 3.9 mW, total spectral drift is 11.5 nm.

The spectral drifts in WGMs of different microdroplets are observed at three relative water humidities of $S_A = 0.753$, 0.8434 and 0.973 and shown in Fig. 3.4a. The solid lines show the experimental results. The diameter ranges of microdroplets are $6.4-8.7$ $\mu$m, $6.4-8.1$ $\mu$m and $7.0-11.1$ $\mu$m for $S_A = 0.7530, 0.8434$ and 0.9730, respectively. The dashed lines show the computational results. We assume that the diameter of the microdroplet is 7 $\mu$m and the temperature of the chamber ($T_\infty$)is 299.55 K. The computational results are consistent with the experimental results. The linear relationship between $\Delta\lambda$ and $P_{inc}$ is clearly observed for both the experimental and computational results. Also the spectral drift is independent of the size of the microdroplets as mentioned. Fig. 3.4c shows the spectral drift calculations made for microdroplets with diameters ranging between $6-12\mu$m. There is a slight difference between the experimental and computational results. For three relative water humidities the computational spectral drifts are smaller than the experimental spectral drifts. The reason of this difference is the omission of the superhydrophobic surface in computing laser-induced heating.

The lumped system equations are used to predict the temperature increase in the microdroplets due to laser heating which can not be measured easily. Fig. 3.4b shows the temperture increase of a 7 $\mu$m diameter microdroplet due to laser heating for three relative water humidities. It can be seen that when $S_A$ decreases the temperature difference between the microdroplets and the chamber increases. Although the increase in temperature is small the spectral drift is large. This makes the photothermal tuning interesting for various applications. The temperature increase for three different-sized microdoplets at $S_A = 0.9730$ is presented in Fig. 3.4d. In spite of the large size difference there is not considerable temperature rise in the microdroplets. This result agrees well with the steady-state solution for the temperature rise in the microdroplet. For the steady-state case, we obtain:

$$T_d - T_\infty = \tilde{Q}_{abs} P_{inc} a^2 / 3 k_g V_m N, \tag{3.6}$$

where $N$ is proportional to $a^3$, and $\tilde{Q}_{abs}$ has approximately linear relationship with $a$. Consequently, the temperature increase is not dependent on $a$.

The reversibility of the tuning mechanism is demonstrated experimentally and computationally. Fig. 3.5 shows the experimental and computational spectral drifts observed from three microdroplets kept at constant relative water humidities. The laser power is

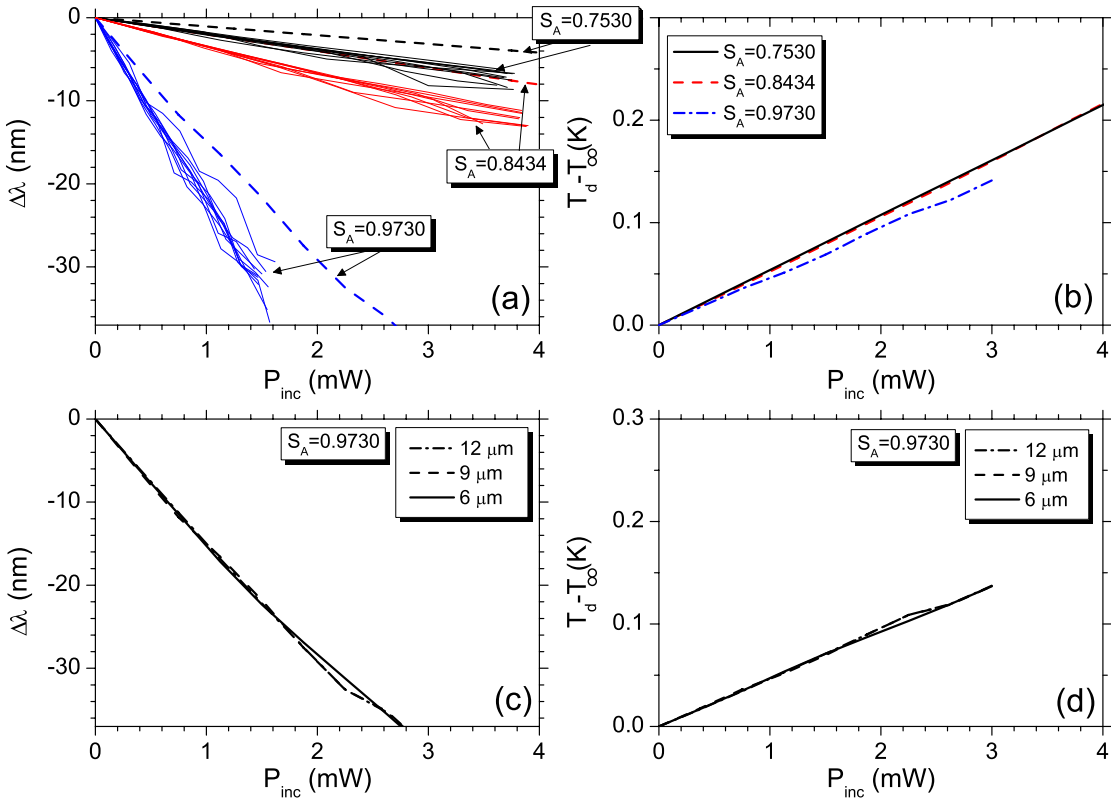


Figure 3.4: (a) Computational (dashed lines) and experimental (solid lines) spectral drifts observed in WGMs at around 590 nm as a function of incident laser power for three different relative water humidities. Computational spectral drifts are calculated assuming 7 $\mu$m microdroplet diameter. Experimental spectral drifts are recorded from different microdroplets with various sizes ranging between $6.4-8.7$ $\mu$m, $6.4-8.1$ $\mu$m and $7.0-11.1$ $\mu$m for $S_A = 0.7530, 0.8434$ and $0.9730$, respectively. (b) Computational results of temperature change of a 7 $\mu$m diameter microdroplet as a function of incident laser power for three different relative water humidities. (c,d) Computational results showing the spectral drifts (c) and temperature changes (d) of 6, 9 , and 12 $\mu$m diameter microdroplets as a function of incident laser power for $S_A = 0.9730$. Curves are hardly distinguishable in (c) and (d) because of large overlaps.

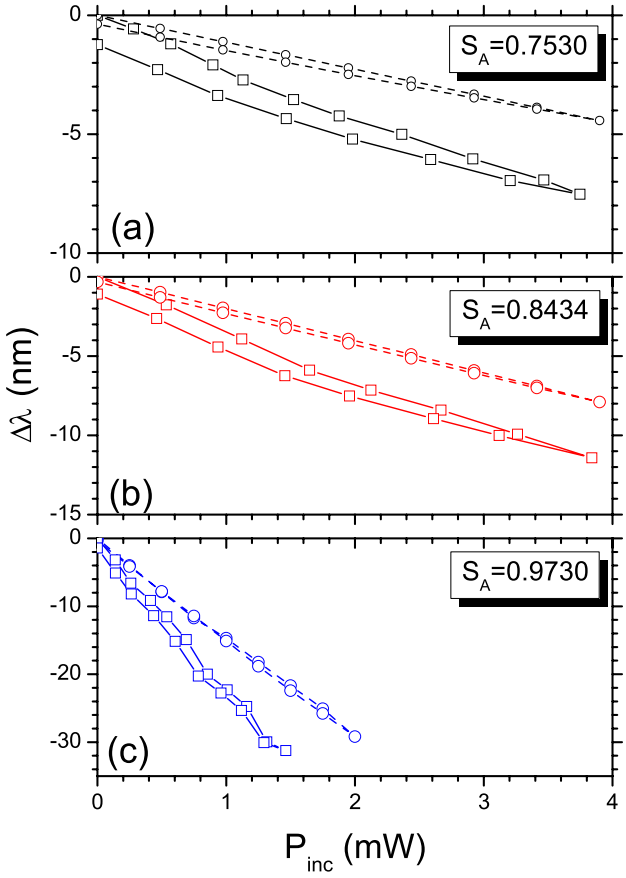


Figure 3.5: The reversibility of spectral tuning for the relative water humidities of (a) $S_A = 0.7530$, (b) $S_A = 0.8434$ and (c) $S_A = 0.9730$. Microdroplet diameters are 6.4, 7.0 and 7.0 $\mu$m in (a), (b), and (c), respectively. The solid lines indicate the experimental data and dashed lines indicate the computational results obtained by assuming that the chamber is initially saturated with glycerol vapor.

increased gradually from zero to a maximum value than decreased gradually from the maximum value to zero. Microdroplet diameters used in the experiment are 6.4, 7.0 and 7.0 $\mu$m for $S_A = 0.7530$, 0.8434 and 0.9730, respectively. Dashed lines show the computational results obtained according to these experimental parameters. The computational results are obtained by assuming that the exposure time of the infrared laser is 8 s at each laser power. This corresponds to average time between two consecutive spectra in our experiment. The spectral tuning of glycerol-water microdroplet is not fully reversible. In other words, the microdroplet does not reach its initial size after the laser is closed. The increase in reversibility by elevating relative water humidity in the chamber implies that the evap-

oration of the glycerol in the microdroplet causes the irreversibility of the spectral tuning mechanism. The differences between the initial and final spectral positions are -1.2, -1.1, and -1.4 nm for $S_A = 0.7530$, 0.8434 and 0.9730, respectively. These correspond to the 16, 9.6, 4.5 percent of the maximum spectral drifts that are -7.5 for $S_A = 0.7530$, -11.4 for $S_A = 0.8434$, -31.2 nm for $S_A = 0.9730$.

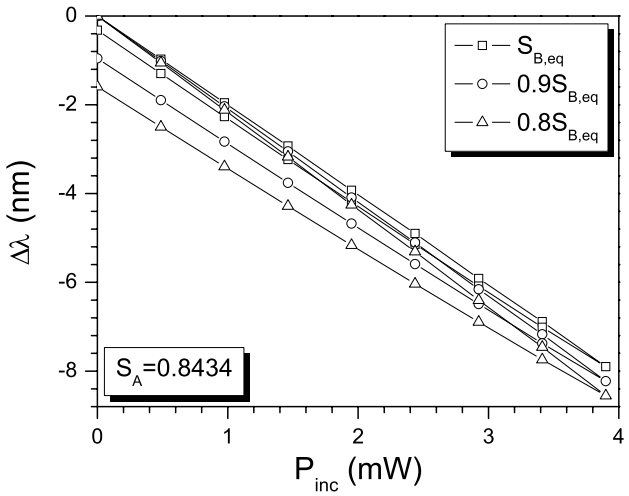


Figure 3.6: The effects of the relative humidity of glycerol vapor on the reversibility of spectral tuning. Computations are performed at $S_A = 0.8434$ for $S_B = S_{B,eq} = 0.0876$ (equilibrium glycerol vapor), $S_B = 0.9S_{B,eq}$ and $S_B = 0.8S_{B,eq}$ assuming a 7 $\mu$m diameter microdroplet. Microdroplet is assumed to be exposed to the infrared laser for 8 sec at each laser power.

The irreversibilities of the computational results are much smaller than the irreversibilities of the experimental results for all three values of $S_A$. The explanation of this difference is that simulations are performed assuming that the relative water humidity of glycerol in the chamber is equal to the relative water humidity of the glycerol in the microdroplet. Fig.3.6 shows the computational results for different equilibrium humidity of the glycerol ($S_{B,eq}$) at $S_A = 0.8434$. When $S_B$ increases toward the equilibrium value, the reversibility increases. For this case, $S_{B,eq}$ is 0.0876. This is computed from the conditions $\gamma_A x_A = S_A$ and $\gamma_B x_B = S_{B,eq}$ at $T_d = T_\infty$.

The transient response of the spectral tuning is analyzed by blocking the mechanical shutter both the infrared laser green lasers. When the shutter is opened, the fluorescence is recorded as the size of the microdroplets increasing. The transient response of 7 $\mu$m micro-

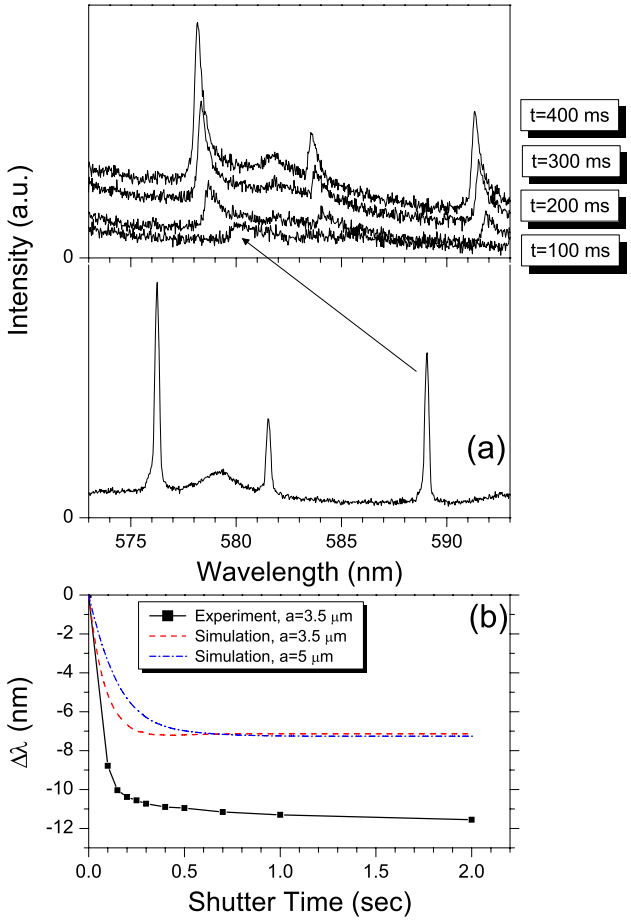


Figure 3.7: Transient analysis of spectral tuning under relative water humidity $S_A = 0.8434$. (a) Fluorescence spectra recorded for a 7.0 $\mu$m diameter microdroplet with no infrared laser excitation (lower plot) and upon exposure of the microdroplet to $P_{inc} = 3.66$ mW infrared laser using 100, 200, 300 and 400 ms shutter times (upper plot). (b) Solid line denotes the spectral shifts observed in (a) as a function of the shutter time. Dashed and dotted lines show the computational results considering $P_{inc} = 3.66$ mW for 7.0 and 10.0 $\mu$m diameter microdroplets, respectively.

droplet is shown in Fig.3.7a. During the experiment, the infrared laser power is 3.66 mW and is kept constant. Also a simulation is performed for two different-sized microdroplets to show the effects of microdroplet size on the time response. By increasing shutter time the drifts of WGMs is increased gradually toward their stable positions. The microdroplet shrinks quickly due to evaporation of water. In Fig.3.7b, the computational and experimental spectral position of a WGM as a function of the shutter time is plotted. In this figure, the measured and calculated maximum spectral drifts are suitable with Fig.3.4a. Also, the measured transient time agrees well with the calculated transient time. Approximately in ∼200 ms, the drift of WGM of 7.0 $\mu$m diameter microdroplet reaches 90% of the total drift. For a 10.0 $\mu$m diameter microdroplet, this transient time increases to ∼ 350 ms. We should indicate that for all states plotted in Fig.3.7, the fully steady state is not obtained. After the shutter is closed, the microdroplet size decreases with a slower rate due to the evaporation of the glycerol.

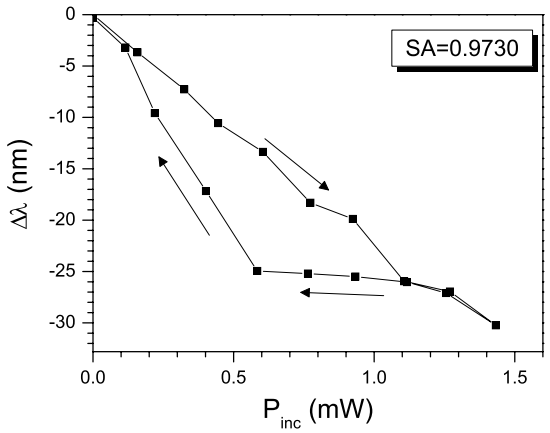


Figure 3.8: Hysteresis in spectral drifts ($\Delta\lambda$) observed for an 11.1 $\mu$m diameter microdroplet. A nearly linear relationship is observed between $\Delta\lambda$ and $P_{inc}$ as $P_{inc}$ is increased from 0 to 1.43 mW while a significant deviation from this linear relationship is observed at about $P_{inc} = 1.11$ mW as $P_{inc}$ is reduced back to zero.

When the infrared power is varied, a hysteretical behavior is observed for relatively large microdroplets due to the WGM resonances observed in laser absorption. An example of the hysteretical behavior is seen in Fig.3.8 for an 11.1 $\mu$m diameter microdroplet. Although the focus point of the infrared laser is the center of the microdroplets, the superhydrophobic surface causes some deviations of the focal spot from an ideal Gaussian. This may cause

WGM resonances in laser absorption plotted in Fig.3.2. While $P_{inc}$ is decreased from a maximum value to zero, the spectral position of WGM is stabilized by such high quality laser absorption. Also this hysteresis behavior is explained in detail in Chapter 4.

### *3.3 Summary*

Spectral tuning of a water-glycerol microdroplet by local heating with a focused infrared laser beam has been demonstrated experimentally by optical spectroscopy and computationally using a lumped system formulation. The experimental results agree well with the theoretical results. The effects of chamber humidity, size of microdroplet are analyzed. It is shown that the deformation due to the optical scattering force is much smaller than the spectral resolution of the experimental setup. Hence the optical scattering force can not be the main reason of large spectral tuning observed experimentally by Kiraz *et al* [39]. The main reason of the size changes is the evaporation of water content in the microdroplet due to laser-induced heating. The spectral tuning does not depend on the microdroplet size and very sensitive to the relative water humidity in the chamber. The slight volatility of glycerol affects unfavorably the reversibility of the spectral tuning mechanism. Also the reversibility increases with increasing relative water humidity of the chamber. The size of the microdroplet determines the transient time of the tuning mechanism. In addition to these results, some hysteresis effects are observed due to WGM resonances in laser absorption.

Chapter 4

# A SALTY WATER MICRODROPLET STANDING ON A SUPERHYDROPHOBIC SURFACE

## *4.1 Introduction*

The slight volatility of glycerol prevents a fully reversible photothermal tuning. An inorganic salt such as NaCl that is nonvolatile and highly soluble in water is used instead of the glycerol. First part of this chapter is the reversible photothermal tuning of NaCl-water microdroplets standing on a superhydrophobic surface. Second part is the experimental and computational demonstration of the photothermal self-stability and optical bistability.

## *4.2 The reversible photothermal tuning of a NaCl-water microdroplet*

In this part, the large spectral tuning of individual NaCl-water microdroplet standing on a superhydrophobic surface was demonstrated. Fig.4.1 shows the spectral drifts measured as a function of the incident laser power for three relative water humidities together with the computational results. The diameters of the microdroplets used in the experiments were between 7$\mu$m and 11$\mu$m. The spectral tuning was independent of the microdroplet size as shown in Fig.4.1. Also the computational results are very sensitive to the contact angle for high humidities.

As shown in Fig.4.1, there is a significant discrepancy between the computational and experimental results for $S_A = 0.973$, when the contact angle increases. The decrease in the quality factor indicates the decrease in the contact angle. The measured average quality factor of the WGMs is 1500 for $S_A = 0.973$,. This value is the almost half of the average quality factor for $S_A = 0.753$ and $S_A = 0.8434$. Additionally, approximations made in the lumped system model and errors in the calculation of $\tilde{Q}_{abs}$ are other sources of errors in the computational results.

The full reversibility of the photothermal tuning mechanism is demonstrated in Fig.4.2. The fluorescence spectra were recorded as the incident laser power ($P_{inc}$) is increased grad-

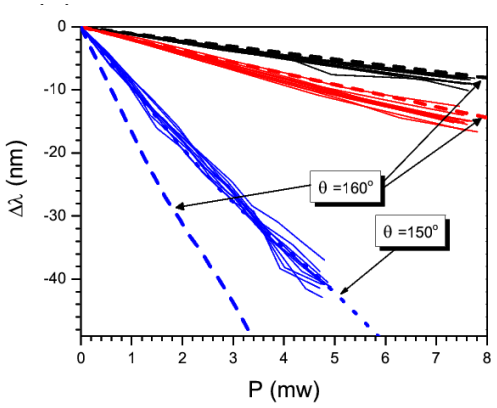


Figure 4.1: Sensitivity of computational (dashed lines) and experimental (solid lines) spectral drifts as a function of infrared laser power for $S_A$=0.7530, 0.8434, 0.9730 respectively. The diameters of the microdroplets are changed between 7-10 $\mu$m. The computational result is the spectral drift for 7 $\mu$m radius.

ually from zero to 7.3 mW and then decreases gradually back to zero. Also the fluctuations in the relative humidity in the chamber were checked by using emission spectra of a second reference microdroplet recorded at the beginning and at end of the each experiment. A maximum blue-shift is observed in the WGMs is observed at 7.3 mW which was the maximum infrared laser power. At the end of the experiment, the total red-shifts in the WGMs of the photothermally tuned and reference microdroplets were 0.06 nm and 0.26 nm, respectively. This means a total reversibility of 1.3 % in photothermal tuning.

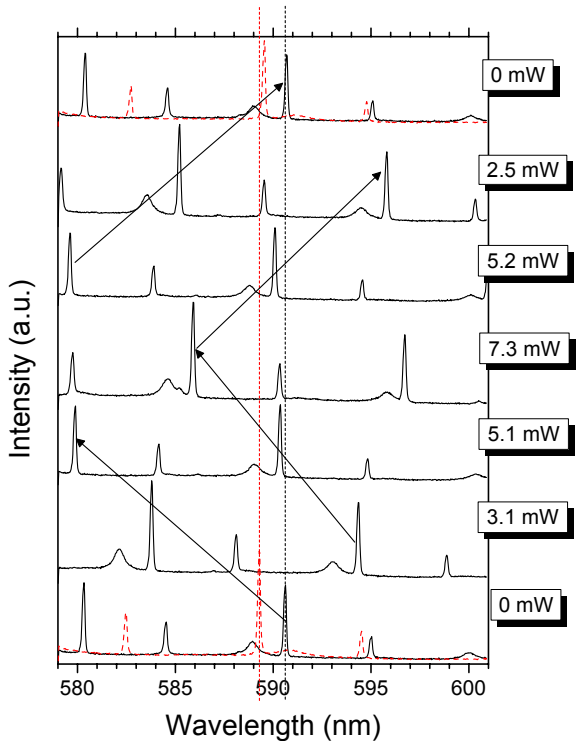


Figure 4.2: Emission spectra recorded from a 8.3 $\mu$m diameter $NaCl$/water microdroplet as the infrared laser power is first increased from and then decreased to zero. Relative water humidity in the experiment is $S_A = 0.8434$. Maximum spectral drift is 15.3 nm at an infrared laser power of 7.3 mW. Dashed spectra are recorded from a 7.1 $\mu$m diameter reference microdroplet that is not unexposed to the infrared laser.

Fig.4.3 shows spectral drift observed the WGMs of three microdroplets as $P_{inc}$ increased and decreased gradually. By considering the reference microdroplet, the reversibilities are calculated as 0 % for $S_A = 0.7530$, 1.3 % for $S_A = 0.8434$, and 0.6 % for $S_A = 0.973$. The reversibilities of NaCl-water microdroplets are much smaller than the irreversibilities in glycerol-water microdroplets.

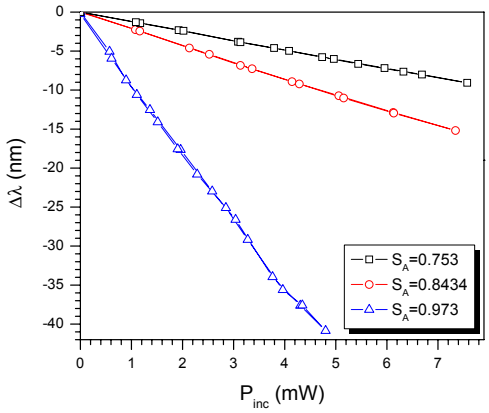


Figure 4.3: Spectral drifts observed in three $NaCl$-water microdroplets as the infrared laser power is first increased from and decreased to zero, for three different relative water humidities. Microdroplet diameters are 8.3 $\mu$m, 8.3 $\mu$m, and 7.7 $\mu$m for $S_A = 0.7530$, 0.8434, and 0.9730, respectively.

The reversibilities of the NaCl-water and glycerol-water microdroplets are compared by recording consecutive emission spectra from each microdroplet. The results of the NaCl-water and glycerol-water microdroplets are shown in Fig.4.4a and Fig.4.4b, respectively. The total delay between two consecutive spectra with the exposure time, readout time of the CCD camera and a 5 s delay is 7.1 s. As shown in Fig.4.4, there is no infrared laser power excitation during the first 30 seconds. Also the constant spectral positions of the WGMs correspond to the high stability of the relative humidity in the chamber. From acquisition 30 to acquisition 140, the NaCl-water microdroplet are heated by the infrared laser at power of 4.6 mW. From acquisition 30 to acquisition 163, the glycerol-water microdroplet are heated by the infrared laser at power of 4.4 mW. At acquisition 30, 10 nm and 8.9 nm blueshifts are observed in the WGMs of the NaCl-water and glycerol-water microdroplets, respectively. The spectral position of the WGMs of the NaCl-water microdroplet is stable between acquisitions 35 and 140. In spite of the infrared laser excitation, the stability of the spectral position indicates that there is no more evaporation in the NaCl-water microdroplet. On the contrary, there is a spectral drift in the WGMs of the glycerol-water microdroplet to the blue wavelengths until acquisition 163 by 10.6 nm. The size of the NaCl-water microdroplet recovers is initial size after infrared laser is blocked at acquisition

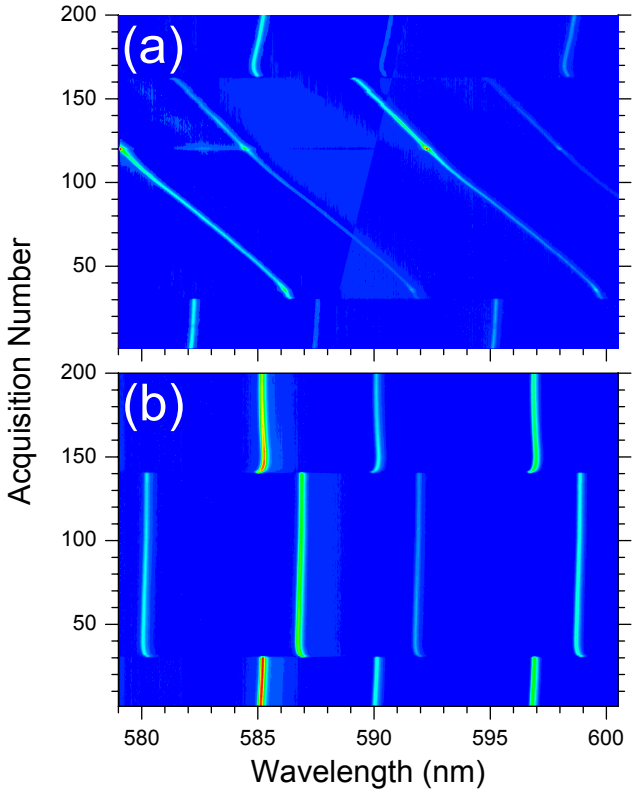


Figure 4.4: Consecutive emission spectra recorded from a 6.5 $\mu$m diameter water-glycerol (a) and 7.7 $\mu$m diameter $NaCl$-water (b) microdroplet. Intensity values in arbitrary units increase from blue to red. Microdroplets are exposed to infrared laser between acquisitions 30-163 and 30-140 in (a) and (b), respectively. Infrared laser power is 4.6 mW and 4.4 mW in (a) and (b). At the end of the on period of the infrared laser, the WGMs of the water-glycerol microdroplet are observed to drift to blue wavelengths. In contrast, the WGMs of the $NaCl$-water microdroplet almost fully recover their initial spectral positions at the end of the on period of the infrared laser.

140. The red-shift in the spectral positions of WGMs of the NaCl-water microdroplet is only 0.05 nm compared to the initial spectral positions. This shows the full reversibility of the photothermal tuning of the NaCl-water microdroplet. In contrast, the spectral difference between the initial and final positions of the WGMs of the glycerol-water microdroplets is almost 10 nm after the laser is blocked at acquisition 163.

### *4.3 Photothermal self-stability and optical bistability of a NaCl-water microdroplet*

Characterization of the ultrahigh quality WGMs of the liquid microdroplets can not be easily managed because of the weakness of the system to the external effects like change in the ambient temperature. Working in constant relative water humidity is the first step of the stabilization of the experimental conditions. A sealed humidity chamber is used for this purpose. At high relative water humidities, the sensitivity due to change in the experimental conditions increases [40]. At this work, we showed a self-stabilization mechanism that stabilizes individual NaCl-water microdroplets more than four hours. Different from our previous works, the individual NaCl-water microdroplets are excited by the focused infrared laser near the vicinity of their rims. Thus we can observe high quality WGM resonances in the infrared laser absorption of water. The infrared laser power is first increased gradually next decreased. A hysteresis curve is obtained during this photothermal tuning round. Hysteresis curves help to detect the self-stabilization points where the volume of the microdroplet is stabilized. In addition to that, the optical bistability which can be used for a microdroplet-based optical memory device is observed.

Optical bistability was observed from a charged isolated glycerol microdroplets in an electrodynamic levitator trap[41, 42]. They used dye-doped salt-water microdroplets. Crystal Violet was used as dye molecule. While tunable-laser wavelength was scanned, they observe hysteresis loops after that they observe bistability explained by evaporation or condensation owing to dye absorption. Also self-stability in the Rhodamine B-doped water microdroplets standing on a superhydrophobic surface was revealed as a result of dye absorption of a green laser [43]. The problem of these experiments was the photobleaching of Rhodamine B. It shortened the stabilization time. The maximum stabilization time that was observed was nearly 2 minutes. In this work, the optical bistability and self-stability of liquid microdroplets are dependent on the infrared laser absorption of water molecules. The stabilization time is not affected by the photobleaching of dye molecule. Thus the photothermal self-stabilization lasts for several hours.

### *4.3.1 Theoretical Hysteresis Curve*

We demonstrated theoretically the photothermal tuning using a lumped system equation between chamber and NaCl-water microdroplet. The modified absorption efficiency ($\tilde{Q}_{abs}$) was calculated using the generalized Lorenz-Mie theory [34, 44]. The refractive index was taken as $n = 1.3544 + 1112.15 \cdot 10^{-9}i$ as shown in Fig.4.5a. The focal waist of the Gaussian beam ($w_0$) was taken as 1000 nm. The molarity of the NaCl amount in the microdroplet at equilibrium is 3.83 M. The real and imaginary parts of the refractive index were determined considering the concentration of salt amount in the microdroplet and the wavelength of the laser [31, 32, 33, 28].

The polarization and propagation directions were along z and x directions, respectively. As shown in the inset in Fig. 4.5 the excitation position of the focused infrared laser was taken 5.5 $\mu$m away from center of the microdroplet along the y direction. Also the angular momentum number and radial mode number of high quality WGMs are indicated in Fig.1a. TM modes can not be excited because of the selected excitation point and the direction of polarization [19]. The computed $\tilde{Q}_{abs}$ function was used to obtain the hysteresis curve and shown in Fig. 4.5. The hysteresis curve exhibits the change in size factor ($\alpha$) as a function of incident power ($P_{inc}$). The power is first increased step by step from 0 to 10 mW, then decreased back to 0 mW. The size parameter range is selected to observe the hysteresis behavior around the high quality $TE_{34}^1$ WGM absorption that is peaked at $\alpha = 29.365$. When $P_{inc}$ is increased the decrease in $\alpha$ is constant until at $P_{inc} = 6.7$ mW. There is a sharp decrease in $\alpha$ owing to the absorption resonance. From $P_{inc} = 7$ mW to $P_{inc} = 10$ $mW$ $\alpha$ again decreases at an nearly constant rate. When $P_{inc}$ is decreased, $\alpha$ increases at a constant rate until $P_{inc} = 1$ mW. At $P_{inc} = 7$ mW, there is a sudden increase in $\alpha$. The lower plateau observed between $P_{inc} = 1$ mW and 7 mW in the photothermal tuning cycle provides the self-stable operation points corresponding to the $TE_{34}^1$ WGM absorption. In the inset of Fig.4.5, the self-stable operation point (red box) is showed on the increasing half of the $TE_{34}^1$ WGM absorption peak. If the size increases or decreases, $\tilde{Q}_{abs}$ will increases or decreases, respectively around the self-stable operation point. These keep the system at the self-stable operation point. Conversely, there is no point like self-stable operation point on the decreasing part of the $TE_{34}^1$ WGM absorption peak as shown in the inset of Fig. 4.5b. Its reason is that the decrease or increase in size corresponds to increase or decrease in $\tilde{Q}_{abs}$,

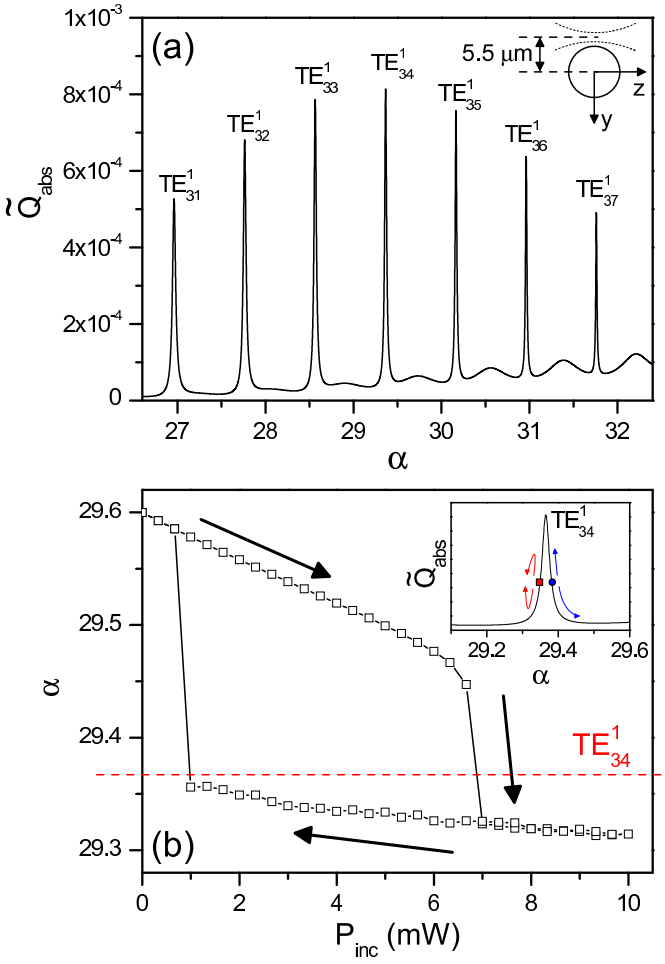


Figure 4.5: (a) The modified absorption efficiency ($\tilde{Q}_{abs}$) as a function of the size parameter ($\alpha$). Calculations are made for a sphere suspended in air by using the localized approximation to the beam-shape coefficients in generalized Lorenz-Mie theory. The laser propagating in z and polarized in x directions is focused near the vicinity of the rim of the sphere at y=5.5 $\mu$m, exciting first order TE modes. (b) The computational hysteresis curve as function of the incident laser power. The dashed line shows the peak position of the $TE^1_{34}$ WGM absorption. Inset shows the sketch of the self-stabilization mechanism.

respectively. The system can not be self-stabilized with a negative slope.

### *4.3.2 Experimental Setup*

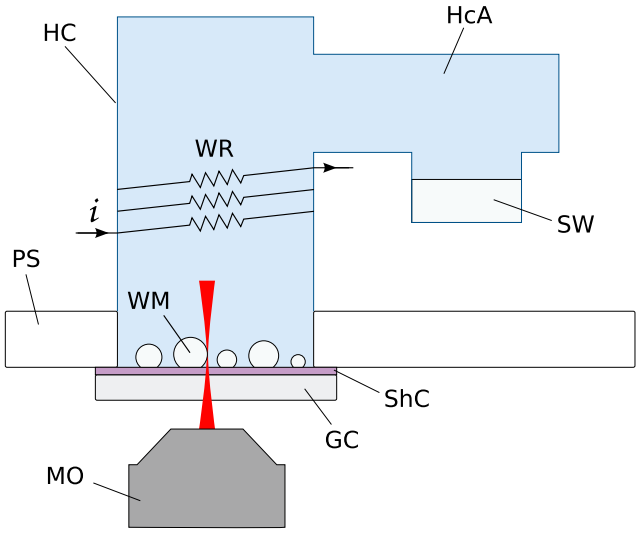


Figure 4.6: Sealed chamber containing the microdroplets (lateral cut). HC : Humidity Chamber. WM : Water Microdroplet. ShC : Superhydrophobic Coating. GC : Glass Cover. SW : Salt Water reservoir. HcA : Humidity-controlled Atmosphere. PS : Plexiglass Support. MO : Microscope Objective. WR : Wire Resistor.

Rhodamine B-doped NaCl-water microdroplets are sprayed on a hydrophobically coated cover glass (Evonik, Aeroxide LE2) using an ultrasonic nebulizer. The initial concentrations of the NaCl and Rhodamine B inside the solution are 2.85 M and 10 $\mu$M, respectively. Then the cover glass is taped under a sealed humidity chamber. The humidity chamber is illustrated in Fig.4.6. A water solution saturated with KCl placed in the small extension of the chamber provides the high and stable humidity of 0.8434 inside the chamber. The microdroplets reach the equilibrium size after several hours. Also there is a wire resistor outside the chamber to heat the air inside the chamber in a controllable way. The current is sent through the wire resistor to test the resilience of the self-stability to the external perturbations.

The optical setup is illustrated in Fig.4.7. A linearly polarized CW infrared laser ($\lambda = 1064\ nm$) is used to heat the individual microdroplet. The maximum output power of the

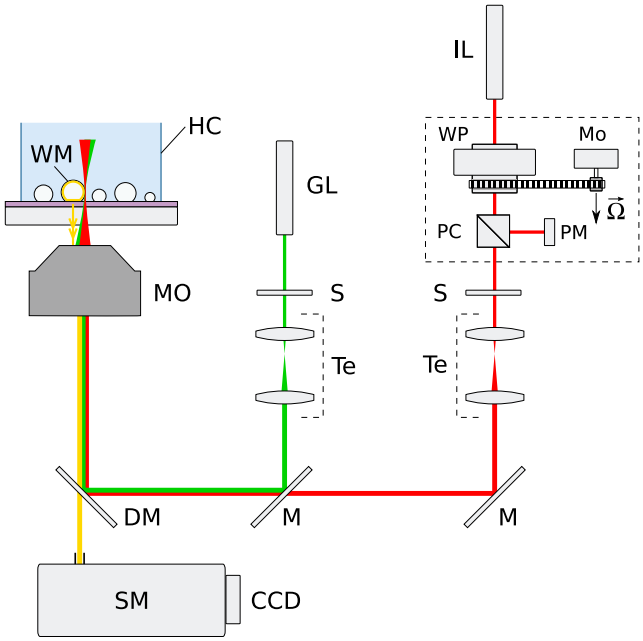


Figure 4.7: Optical setup. From lasers to sample ; IL : infrared laser. WP : ball bearing-mounted waveplate. SM : step motor. PC : polarizing cube. PM : power meter. GL : green laser. S : electromechanical shutter. Te : telesope. M : mirror. DM : dichroic mirror. MO : microscope objective. HC : humidity chamber (partially drawn). WM : water microdroplet. DM : dichroic mirror. SM : spectrometer. CCD : spectrometer imaging sensor.

laser is 300 mW. A half-waveplate for changing the infrared laser power is placed inside a computer-controlled step motor. The infrared laser beam is divided into two by a polarizing cube beam splitter. The undeflected and deflected outputs of the cube are sent to the experiment and to a photodetector, respectively. The photodetector is used to measure the power of the infrared laser. A power calibration is done before every experiment by detecting the power. The power at the photodetector is measured for different waveplate angles as a power calibration before each experiment. The power is adjusted accurately and reversibly by this computer-controlled system. Additionally, a mechanical shutter and a telescope are placed in the path of the infrared laser. A CW green solid state laser ($\lambda = 532\ nm$) is used to excite the Rhodamine B dye in the microdroplet. A mechanical shutter is placed in the path of the green laser to control the excitation time and to prevent photobleaching. The range of the laser powers are between 1-10 $\mu$W for green laser and 1-10 mW for infrared laser at the focus of the microscope objective.

The infrared and green lasers beams are merged by a beam splitter and come to an inverted microscope. The incoming beam is reflected off a dichroic mirror. An oil objective (NA=1.4,60x) is used to focus the beam to the rim of the microdroplet standing on the superhydrophobic surface in the inverted geometry. The same objective is used to collect the fluorescence from the Rhodamine B molecules. A spectrometer composed of a 50 cm monochromator and a CCD camera (spectral resolution of 0.15 nm around 590 nm and 1.5 s readout time) records the fluorescence. The green laser is opened during 500 ms exposure time for all the spectra recorded in the experiment.

### *4.3.3 Results*

*Experimental Hysteresis Curves*

The emission spectra recorded form a 14 $\mu$m diameter NaCl-water microdroplet is shown in Fig.4.8a. The spectral position of WGM A indicated in Fig.4.8a is seen in Fig.4.8b as a function of the incident laser power ($P_{inc}$) during two consecutive tuning cycles. Firstly, $P_{inc}$ is increased gradually from its minimum value to its maximum value and then decreased back to the minimum value. A horizontal plateau is seen for both tuning cycles. The stable position is stable at around 583.1 nm as $P_{inc}$ is decreased from it s maximum value. This position indicates the self-stable operation point. If we compare the experimental hysteresis curves in Fig.4.8b with the theoretical hysteresis curve in Fig.4.5 which we assumed that the diameter of the microdroplet is 10 $\mu$m, a difference in the flatness of the curves is observed due to the high quality of the absorption resonances which gave rise to the self-stable operation in the experiment. This result is compatible with the Ref.[45]. There is a small offset between two experimental hysteresis curves while $P_{inc}$ is increased owing to variations in the chamber atmosphere. In spite of this offset, the spectral position of the self-stable operation point does not change because of the unchanged refractive index of the microdroplet between consecutive photothermal tuning cycles which causes to the stable operation. Thus, the constant spectral position indicates the self-stable operation. In addition to that, a sudden spectral jump is observed at around $P_{inc}$=0.78 mW while infrared laser is decreased due to the multiline spectrum of the diode pumped solid state infrared laser used in the experiments.

The free spectral range of the microdroplet in Fig.4.8a and in Fig.4.8b is approximately

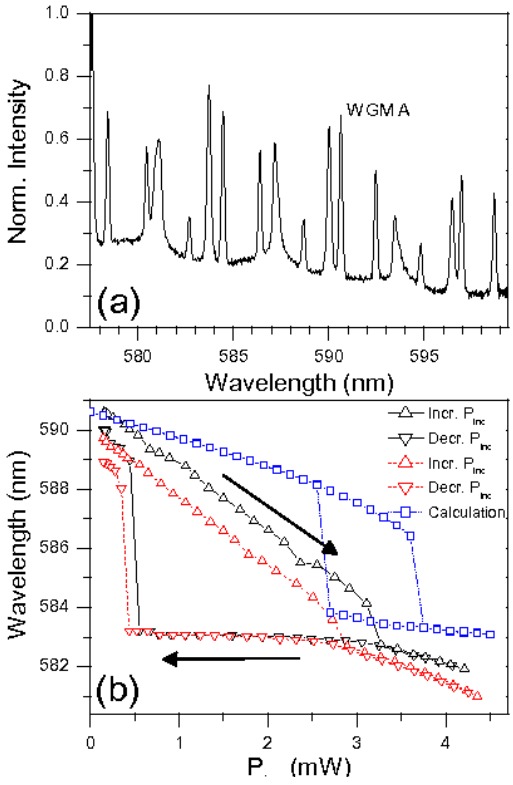


Figure 4.8: (a) Normalized emission spectrum recorded from a 14 $\mu$m diameter NaCl-water microdroplet. (b)Triangles show the hysteresis curves obtained by plotting the change in the spectral position of WGM A during two consecutive photothermal tuning cycles. The horizontal plateau observed at 583.1 nm as $P_{inc}$ is decreased corresponds to the self-stable operation point in both hysteresis curves. Fluctuations in the ambient atmosphere lead to a drift between the consecutive hysteresis curves. No drift is observed at the self-stable point. Squares show the calculated hysteresis in the spectral drift of the $TM^1_{89}$ WGM. The horizontal plateau at 583.9 nm shows self-stabilization due to the absorption of the 1064 nm laser by the $TE^1_{47}$ WGM.

8 nm. The real part of refractive index of the NaCl-water aqueous solution is 1.3677 at around 590 nm [28]. The WGMs of this microdroplet correspond to first order WGM of a microdroplet with $a = 6.6733$ $\mu$m. WGM A is well matched with $TM_{89}^{1}$ mode. In addition to the experimental hysteresis curves, a computational hysteresis curve is shown in Fig.4.8a by considering that the refractive index at 1064 nm is $n = 1.3544 + 1112.15 \cdot 10^{-9} i$. We assumed that the excitation point of the infrared laser is the rim of the microdroplet with a focal waist of $w_0$=1000 nm. A horizontal plateau is seen at around 583.9 nm. This corresponds to the self-stable operation. There are some differences between the experimental hysteresis curves and the computational hysteresis curve. The main difference is the position of the spectral horizontal plateau. Some reasons of these differences are the calculation errors in radius determination by mode-matching, the variations of the refractive index at different wavelengths, the variation of the position of the focus spot in the experiment and the assumptions made in the lumped system formulation.

*Resilience to an External Perturbation*

In this part the resilience of the self stability to an external perturbation is demonstrated. As an external perturbation, the ambient atmosphere of the chamber is heated by a wire resistor around the chamber glass for 3 s at 4.25 W. The results are showed in Fig.4.9 where 80 consecutive spectra is recorded from an 18 $\mu$m droplet at 2.5 s intervals. In Fig.4.9a there is self-stabilization. In Fin.4.9, there is no self-stabilization. As a result of self-stabilization, the spectral positions of WGMs do not change due to the external heating of the chamber atmosphere. On the contrary, there is a blue-shift of 4.8 nm after 65 spectra in Fig.4.9b due to external heating.

Also, we simulate the resilience of the self-stability to an external perturbation and the result is shown in Fig.4.9c. In these simulations, $S_A$ is increased step by step from 0.8434 to 0.8477 for two cases. In the first case, there is no self-stabilization. As a result of the increase in $S_A$ at 5 s intervals, a decaying exponential in the relative wavelength shift is observed like the experimental result in Fig. 4.9b assuming that the infrared laser power is zero and the initial radius of the microdroplet is 5.0735 $\mu$m. In the second case, self-stabilization exists so that the relative wavelength shift is almost zero with the time due to the increase in $S_A$. For this simulation, the calculations are made by using the same

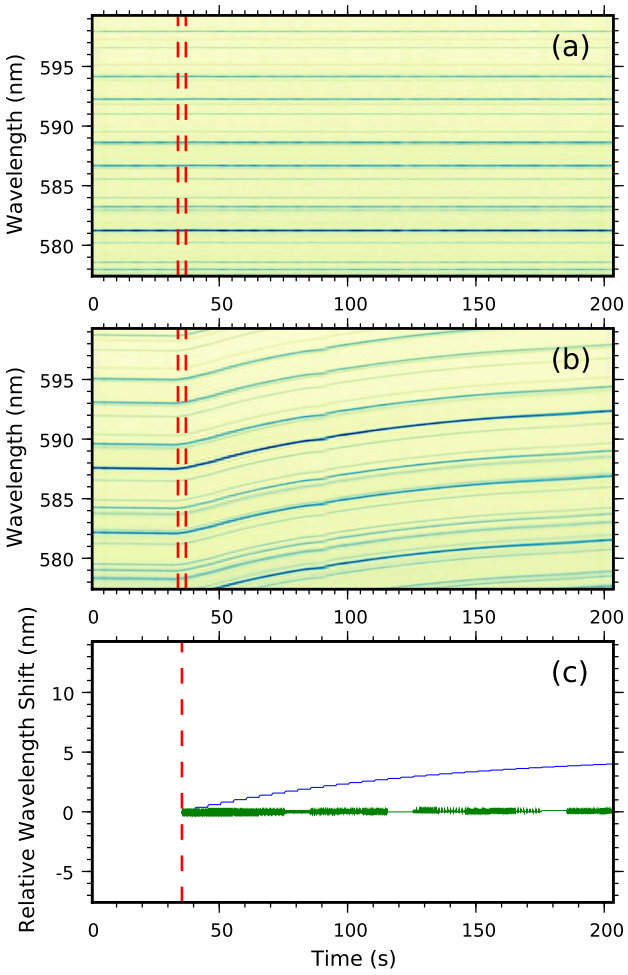


Figure 4.9: Wavelength stability of a group of WGMs from a 18 $\mu$m diameter NaCl-water microdroplet undergoing an external heating perturbation, with accumulated spectra taken at 2.5 $s$ intervals. (a) Microdroplet locked into self-stable operation. The effect of the perturbation (dashed lines) is barely seen. (b) Regular (unlocked) operation. The perturbation initiates a marked drift to the blue of the WGM wavelengths. (c) Calculations showing the spectral drift of the WGMs at around 590 nm as a result of gradual increase in $S_A$ from 0.8434 to 0.8477 in the absence and presence of self-stabilization.

parameters used for Fig.4.5. The laser power and the structure factor are selected to be 5.67 mW and 29.639 nm, respectively. The relative spectral drift observed in the simulation results for the absence of the self-stabilization is $\sim 4$ nm. The maximum spectral drift for the other case is $\sim 0.2$ nm. The simulation results agree well with the experimental results. However, the experimental spectral drift is smaller than the calculated spectral drift for the stabilized case. The main reason of this difference is attributed to the lower quality factor of the absorption resonances owing to the larger microdroplet.

*Long Time Self-Stabilization*

The self-stabilization can last for a long time. Fig.4.10 shows the hysteresis curve and the consecutive emission spectra recorded from a 14 $\mu$m diameter microdroplet when it was self-stabilized and it was not self-stabilized. There are two self-stable operation points in Fig.4.10a around 585.4 nm and 590.3 nm. After we obtained the hysteresis curve, the microdroplet was self-stabilized at 585 nm which is the first self-stabilization point in Fig.4.10a . Consecutive emission spectra were recorded when it was locked and it is shown in Fig.4.10b. $P_{inc}$ value was 2.02 mW and it was constant during the experiment. As seen in Fig.4.10b, there is no spectral drift in the positions of the WGMs during one hour. We can not obtain the spectral drift less than 0.15 nm owing to our experimental resolution limit. The maximum locking time was larger than 90 minutes. We recorded the consecutive emission spectra from the same microdroplet when it was not self-stabilized and the result is shown in Fig.4.10c. $P_{inc}$ value was 0 mW during the experiment. As seen in Fig.4.10c, the spectral positions of the WGMs drift owing to the variations in the ambient atmosphere in the chamber.

If we compare the result of these experiments with the recent work about the self-stabilization depending on the dye absorption [43], the large increase in the maximum stabilization time can be seen obviously. The problem of self-stabilization depending on the dye absorption is the photobleaching of the Rhodamine B dye. Because of the photobleaching, the maximum self-stabilization time was only a few minutes. In this work, the self-stabilization mechanism depends on the water absorption at 1064 nm. Hence, there is no limiting factor of the self-stabilization time like photobleaching. But due to their liquid nature, the microdroplets are very sensitive to the fluctuations in the ambient atmo-

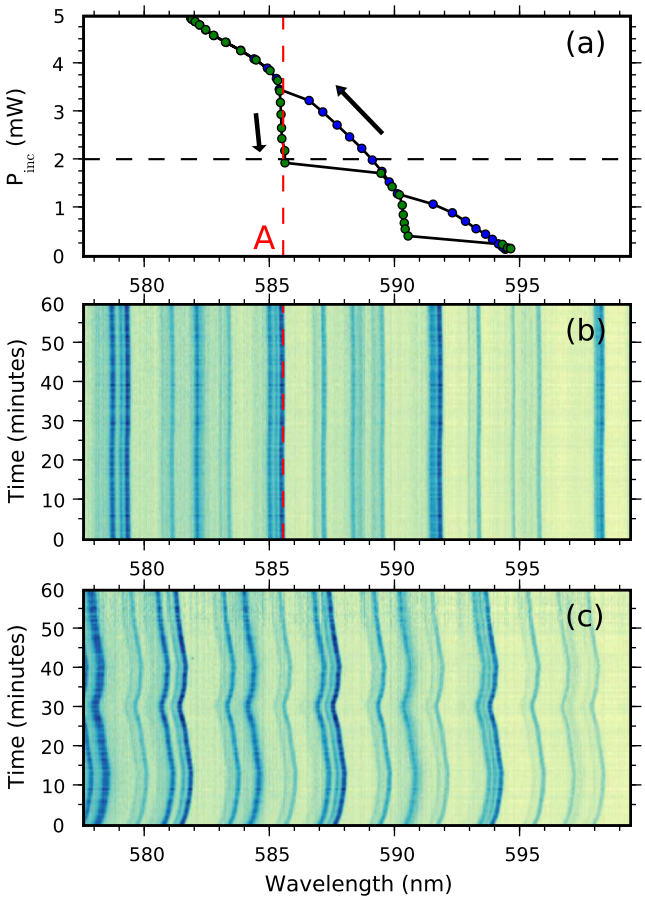


Figure 4.10: Long time stability of WGMs from a 14 $\mu$m diameter microdroplet. (a) Hysteresis curve obtained by following a WGM in the emission spectra recorded from the microdroplet, in which two self-stable operation points exist. Blue and green circles indicate increasing and decreasing $P_{inc}$, respectively. (b) Time-accumulated spectra for the microdroplet locked at $P_{inc}$=2.02 mW (dashed red line). No spectrum change is observed for an hour. (c) Time-accumulated spectra for the same microdroplet, unlocked ($P_{inc}$=0 mW). The WGMs drift slowly. The number of spectra in (a) and (b) is 112.

sphere. Providing the stable chamber conditions by using an external active temperature stabilization system, the maximum self-stabilization time can be increased easily.

*Optical Bistability*

We also observe optical bistability of the liquid microdroplet by using the hysteresis curves. In a hysteresis curve, the size of the microdroplet is different at the same infrared laser power during the photothermal tuning cycle as shown in Fig.4.11a. The spectral position

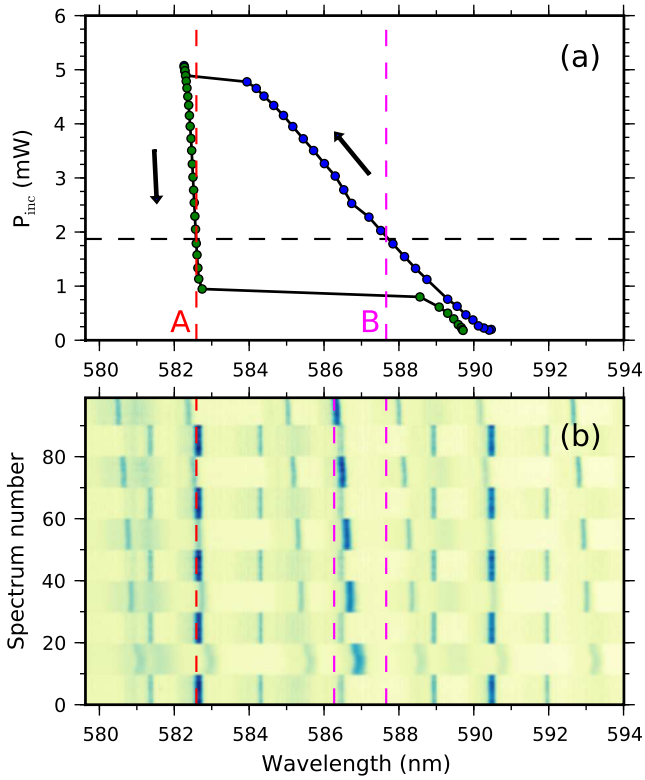


Figure 4.11: Optical bistability observed from a 12 $\mu$m diameter microdroplet. (a) Hysteresis curve obtained by following a WGM in the emission spectra recorded from the microdroplet. Blue and green circles indicate increasing and decreasing $P_{inc}$, respectively. (b) Time-accumulated spectra for the same microdroplet exhibiting bistable behavior, recorded at $P_{inc}$=1.87 mW. The delay between consecutive spectra for a given state (A or B) is 2.5 s. Additional delay when switching between states is 1 s from A to B, and 8 s from B to A.

of WGM in Fig.4.11a is stable in spite of decreasing infrared laser power. It indicates that there is a self-stabilization point at state A. At spectral position of state B, the curve changes with the increasing infrared laser power. It shows the absence of the self-stabilization. An

experimental procedure is applied to switch reversibly between state A and state B. When the microdroplet is self-stabilized at position of state A, the infrared laser is blocked for ∼500 ms then unblocked. It is very easy to come back to state A from state B by increasing and decreasing the infrared laser. This procedure can be achieved repeatedly. Repetitive switching between position of state A and position of state B is demonstrated by recording consecutive emission spectra and shown in Fig.4.11b. Optical bistability between two states is clearly seen in Fig.4.11b. The spectral position of state A is stable and it shows the presence of the self-stabilization. The spectral position of B becomes close to the position A after each switching procedure. After 9 switching procedure, the total spectral drift of B is ∼1.5 nm. In spite of the 1.5 nm spectral drift of B, there is an obvious spectral position difference between A and B. The spectral drift of B can be prevented by using a conventional temperature stabilization feedback circuit using a Peltier element and a temperature sensor. Therefore, two states can be distinguishable for all times by keeping stable the spectral position of unstabilized state B.

### *4.3.4 Summary*

Consequently, a self-stabilization mechanism for NaCl-water microdroplet standing on a superhydrophobic surface was shown. This mechanism was resilient to the variations of the ambient atmosphere. Also computational self-stabilization was obtained by using the lumped system model with Lorentz-Mie theory. The self-stabilization could last for several hours because it was independent of the dye absorption. Additionally, a repeatable optical bistability was demonstrated between the locked and unlocked states.

Chapter 5

# SPECTRAL TUNING OF LIQUID MICRODROPLETS STANDING ON A SUPERHYDROPHOBIC SURFACE USING ELECTROWETTING

## *5.1 Introduction*

Largely tunable optical microcavities are essential for optical communications systems that use light and that are formed from largely tunable optical switches and filters [1]. Generally solid optical microcavities which are produced by microfabrication methods are used. Also liquid microdroplets standing on a superhydrophobic surface that are easily deformable because of their liquid nature can be thought as alternative optical microcavities for such applications. Other advantages of liquid microdroplets are their cost-effective and disposable nature. The sphericity of the microdroplets and the position stabilization are obtained with using superhydrophobic surfaces that are not complex like electrodynamic levitation and optical tweezing. There are different techniques to change the size and shape of the microdroplets. One of them is electrowetting.

## *5.2 Theory*

Manipulating droplets which are standing on surfaces can be possible by controlling the interfacial energies [46]. At the liquid-vapour interface, the temperature gradients and gradients in the concentration of surfactants increase the interfacial energies. By the thermocapillary and Marangoni effects this increase in interfacial energies can be used to move the droplets on surfaces. One way to increase the interfacial energies is electrowetting. Electrowetting is the rise of the wetting of the solid surfaces by liquid microdroplets due to an external electric field. The microdroplets are conductive because of salt content. The outside medium of the microdroplet can be either air or oil. The only factor that determines the behavior of the microdroplet is the surface tension if there is no external electric field. The droplet shape is dependent on the free energy $F$. The summation of the areas $A_i$ of the

interfaces between three phases gives the free energy. These phases are the solid substrate (s), the liquid droplet (l) and the ambient phase (v).

### *5.2.1 Young's Equation*

The basic equation for qualitative analysis of wettability of solid surfaces is Young's equation. There are two cases for a microdroplet standing on a surface:

1. Complete spreading on the surface (contact angle $\theta = 0$).

2. Contact angle is finite.

In the second case, the wetting line or three-phase contact line is developed. The interfacial tensions relates with contact angle by Young's Equation.

$$cos\theta_Y = \frac{\sigma_{sv} - \sigma_{sl}}{\sigma_{lv}} \tag{5.1}$$

where $\sigma_{sv}$ is the solid-vapour surface tension, $\sigma_{sl}$ the is solid-liquid surface tension and $\sigma_{lv}$ is the liquid-vapour surface tension.

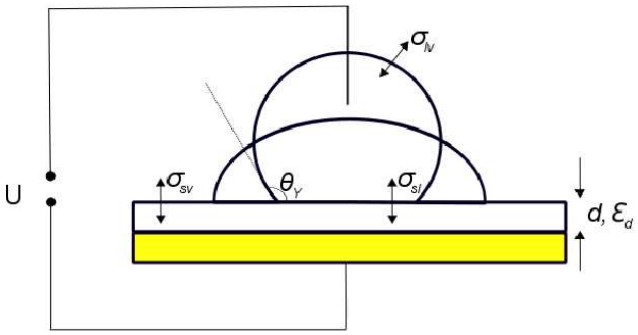


Figure 5.1: General electrowetting setup. $\sigma_{sv}$ : solid-gas surface tension, $\sigma_{sl}$ : solid-liquid surface tension, $\sigma_{lv}$ : liquid-gas surface tension, $\theta_Y$ : contact angle, U : applied voltage

If $\sigma_{sv}$ is higher than $\sigma_{sl}$, the right hand side of Eq. 5.1 will be positive so the contact angle is smaller than $90^o$. The solid is wetted by liquid partially. Otherwise, if $\sigma_{sv}$ is less than $\sigma_{sl}$ ($\sigma_{sv} < \sigma_{sl}$), $cos\theta$ will be negative. The contact angle have to be greater than $90^o$.

### *5.2.2 The contact angle change due to an external electric field*

A space charge layer of counter ions is formed due to an applied voltage ($dU$) near the superhydrophobic surface. The effective interfacial tension ($\sigma_{sl}^{eff}$) decreases because of the adsorption of surfactant molecules at an air-water interface:

$$d\sigma_{sl}^{eff} = -\rho_{sl} dU, \tag{5.2}$$

where $\rho_{sl}$ is the surface charge density of the counter-ions and changes with the applied voltage U. A simplifying assumption is made to find the voltage dependence of $\sigma_{sl}^{eff}$. According to the assumption, all counter-ions are positioned at a fixed distance $d$ from the surface. In this model, the capacitance per unit area of the double layer is $c = \epsilon_0\epsilon_1/d$, where $\epsilon_1$ is the dielectric constant of the liquid. The integral equation is obtained:

$$\sigma_{sl}^{eff}(U) = \sigma_{sl} - \int_{U_{pzc}}^{U} \rho_{sl} d\widetilde{U} = \sigma_{sl} - \int_{U_{pzc}}^{U} c\widetilde{U} d\widetilde{U} = \sigma_{sl} - \frac{\epsilon_0\epsilon_1}{2d}(U - U_{pzc})^2, \tag{5.3}$$

where $U_{pzc}$ is the potential of zero charge. The effect of applied voltage to the contact angle is obtaion by inserting Eq. 5.3 into Eq. 5.2. For a system shown in Fig.5.1, the contact angle response evolves by:

$$cos\theta = cos\theta_Y + \frac{\epsilon_0\epsilon_1}{2d\sigma_{lv}}(U - U_{pzc}). \tag{5.4}$$

## *5.3 Experimental Setup*

The experimental setup is demonstrated in Fig. 5.2. The chamber consisted of two indium tin oxide (ITO) coated cover glasses. This ITO coating makes the surface of the cover glass conductive. The nonconductive surface of the coverglass was coated with superhydrophobic silica nanoparticles (Degussa A.G., LE2) . The silica nanoparticles were dissolved in ethanol. The ethanol dispersion in the solution was 50 mg/ml. Glycerol-water microdroplets were sprayed onto the superhydrophobic surface using an ultrasonic nebulizer. Glycerol to water ratio in the solution was 10/90. Also, the solution contained 5 $\mu$M rhodamine B dye and 135 mM KCl. After the microdroplets were sprayed on the superhydrophobic surface, two ITO coated coverglass were glued to each other to form a sealed chamber. The top

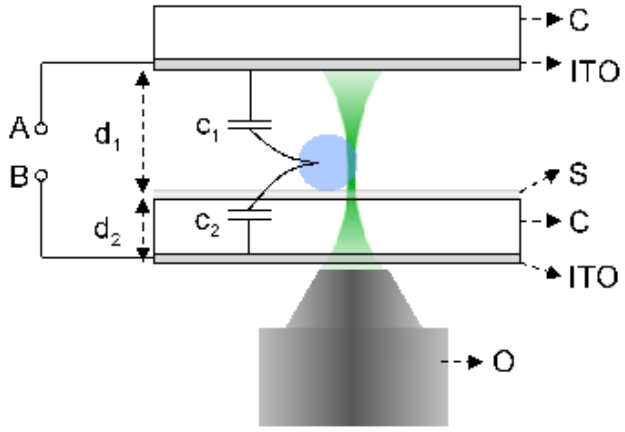


Figure 5.2: Illustration of the experimental setup. C, cover glass; S, superhydrophobic coating; ITO, indium tin oxide coating, O, microscope objective. The sketch is not to scale. c1 and c2 indicate capacitances per unit area.

and bottom surfaces of the chamber were conductive and nonconductive, respectively. The separation between two cover glasses were obtained between 30 $\mu$m and 60 $\mu$m. The chamber which used for the results of this work had a 40 $\mu$m separation. The potential difference between the node A and the node B was positive ($V_{AB} \geq 0$). Similar results were observed for $V_{AB} \leq 0$ due to the characteristics of the electrowetting. The individual microdroplets were excited near the vicinity of their rims with a green solid state laser ($\lambda = 532\ nm$). The spectral positions of the WGMs were followed by using the emission of the Rhodamine B under laser excitation. The air microscope objective (NA=0.8, 60X) was used in the experiment in the inverted geometry. The collection of fluorescence signal was done by the same objective. The signal was detected by a charge coupled device (CCD) camera then came to a 0.5 m monochromator (600 grooves/mm grating). The spectral resolution of the CCD camera was 0.15 nm. The fluorescence spectra are recorded during an exposure time of 0.5 s.

### *5.4 Results*

Our experimental configuration is different than the classical electrowetting setup. Since the voltage is not applied directly to the microdroplet at our experimental setup so the actual potential difference between the microdroplet and the conducting layer is not the same as the applied voltage. The relation between the actual potential difference ($U$) and the applied voltage ($V_{ab}$) evolves by

$$U = V_{ab} c_{eq}/c_2, \tag{5.5}$$

where $c$ denotes the capacitance per unit area. The equivalent capacitance can be defined in terms of $c_1$ and $c_2$ (shown in Fig. 5.2) as $c_{eq} = c_1 c_2/(c_1 + c_2)$.

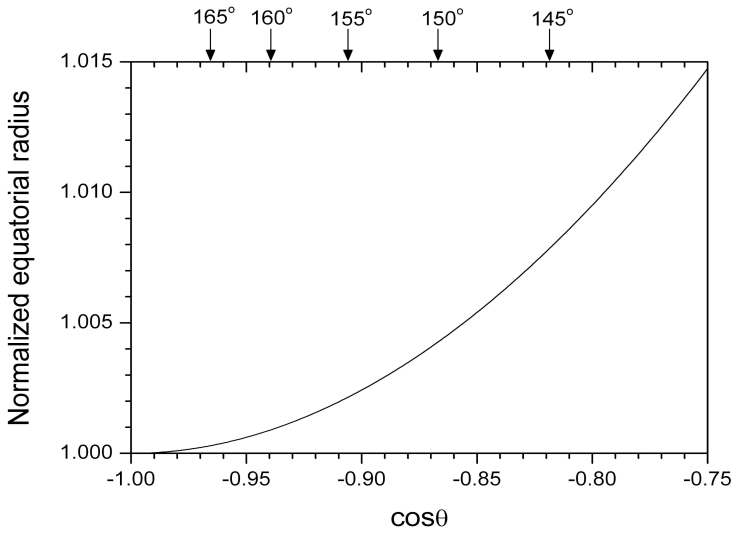


Figure 5.3: Normalized equatorial radius versus cosine of the contact angle of an ideal truncated sphere with constant volume. Contact angles are indicated with arrows.

For an ideal truncated sphere that has constant volume, the normalized equatorial radius depends on cos$\theta$ as shown in Fig. 5.3. Due to small changes in contact angle, this curve

can be considered as linear. In addition to that, for large mode numbers, there is a linear asymptotic relationship between the spectral position of the WGMs ($\lambda$) and $r$ [30]. Thus, a parabolic dependence can be assumed between $\lambda$ and $V_{AB}$ for small changes in the contact angle. For a microdroplet standing on a superhydrophobic surface, the contact angle is approximately 150°. According to the $\theta = 150°$ , the spectral shift as a function of the applied voltage evolves by

$$U = \lambda_0 + 0.032\lambda_0 \frac{\epsilon_0 \epsilon_d c_{eq}^2}{d_2 \sigma_{lv} c_2^2} V_{AB}^2, \tag{5.6}$$

where $c_1 = \epsilon_0/d$, $c_2 = \epsilon_0\epsilon_d/d_2$, $\epsilon_0 = 8.854 \times 10^{-12}\ Nm^2/C^2$, $\epsilon_d = 4.6$ for Borosilicate glass, $d_2 = 605\ nm$, $\sigma_{lv} = 0.064\ N/m$ for glycerol and $\lambda_0 = 605\ nm$. Then, the following relationship is obtained:

$$\lambda = \lambda_0 + 1.53 \times 10^{-5} V_{AB}^2. \tag{5.7}$$

Eq. 5.7 is independent of r and in units of nanometers.

The consecutive emission spectra recorded from 6.5 $\mu$m microdroplet is shown in Fig.5.4. $V_{AB}$ is increased step by step from 0 to 400 V. A redshift is noticeably observed in the WGMs as $V_{AB}$ is increased. The maximum redshift of the WGM A is 3.3 nm at 400 V. Assuming the unbiased contact angle is 150° and using Eq.5.7, the increase in the equatorial radius and the decrease in the contact angle is found 18 nm and $\approx 7°$ , respectively. Also, the quality factor of the WGM A decreases from 3500 at 0 V to 2500 at 400 V.

Fig.5.5 shows the consecutive emission spectra from a 7.1 $\mu$m microdroplet in the same sample. $V_{AB}$ is increased to 400 V, then decreased gradually back to zero. Although maximum applied voltage is same for two microdroplets, the redshift of WGM B of this microdroplet is 6.72 nm. It is about two times larger than the redshift of WGM A. This increase in spectral shift is attributed to the different contact angles between microdroplets and surface. Also at high voltages, the line shape of WGM B seems more worse than the line shape of WGM A.

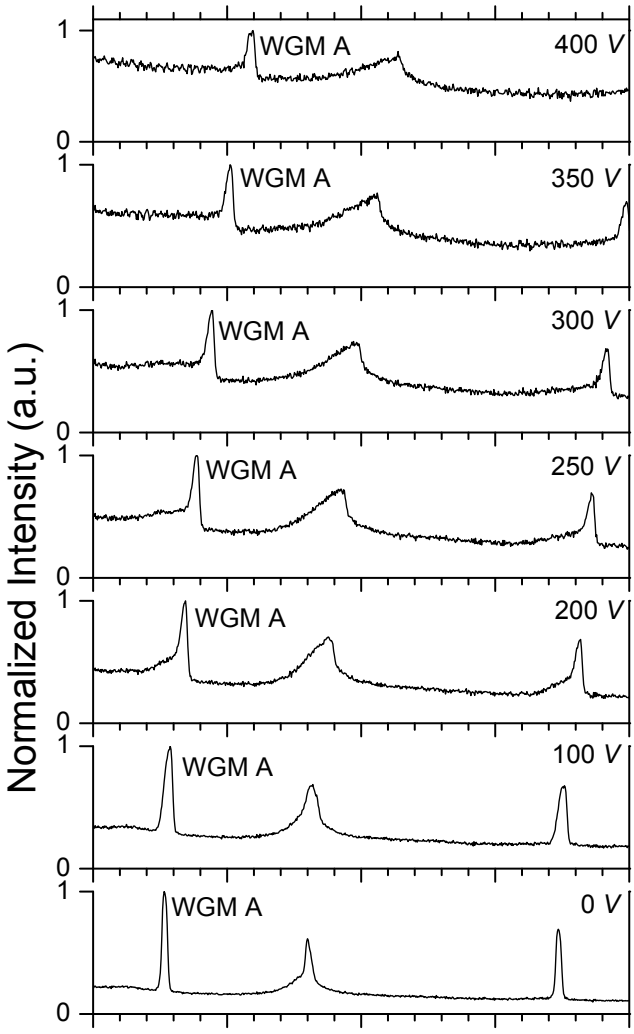


Figure 5.4: Normalized emission spectra recorded from a 6.5 $\mu$m diameter microdroplet while the voltage is gradually increased from 0 to 400 V. At 400 V a maximum red shift of 3.3 nm is observed in the WGM A. At high voltages a blue shoulder is seen in the WGMs.

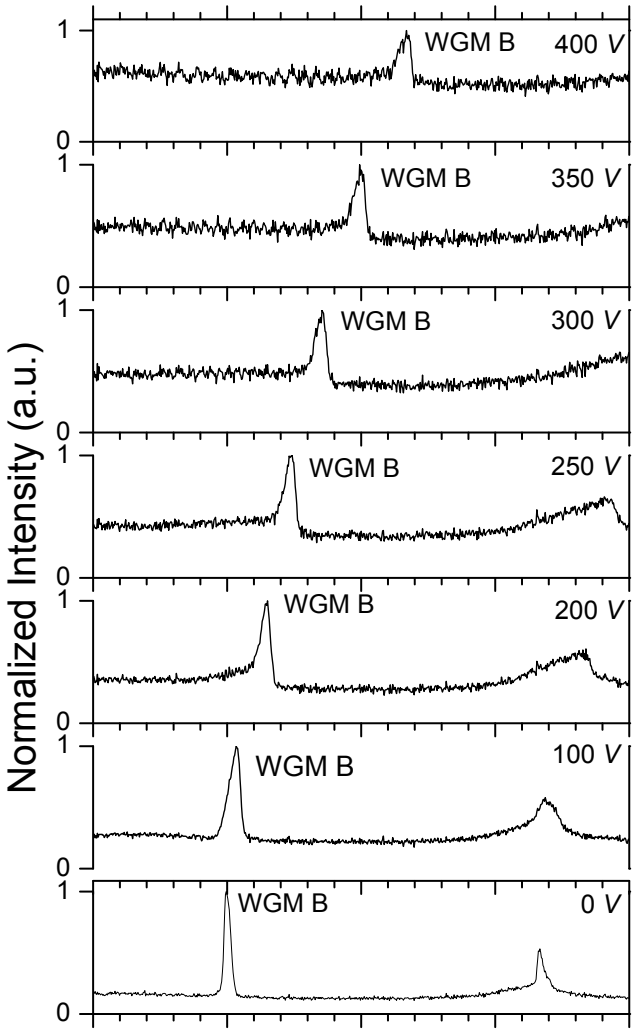


Figure 5.5: Normalized emission spectra recorded from a 7.1 $\mu$m diameter microdroplet while the voltage is gradually increased from 0 to 400 V. At 400 V a maximum red shift of 6.7 nm is observed in the WGM A. At high voltages a blue shoulder is seen in the WGMs.

An asymmetry is observed at the line shape of the WGMs at high bias voltages. Blue shoulders arise due to this asymmetry. The reason is that electrowetting causes the non-sphericity of the microdroplet toward an oblate spheroid [47]. The degeneracy between the WGMs of an oblate spheroid which has different azimuthal mode numbers is lifted. A blueshift is seen on the WGMs that have lower azimuthal numbers. These WGMs do not circulate in the equatorial plane. Although the microdroplets are excited near the vicinity of their rims, the WGMs that have lower azimuthal mode numbers can be excited by residual coupling.

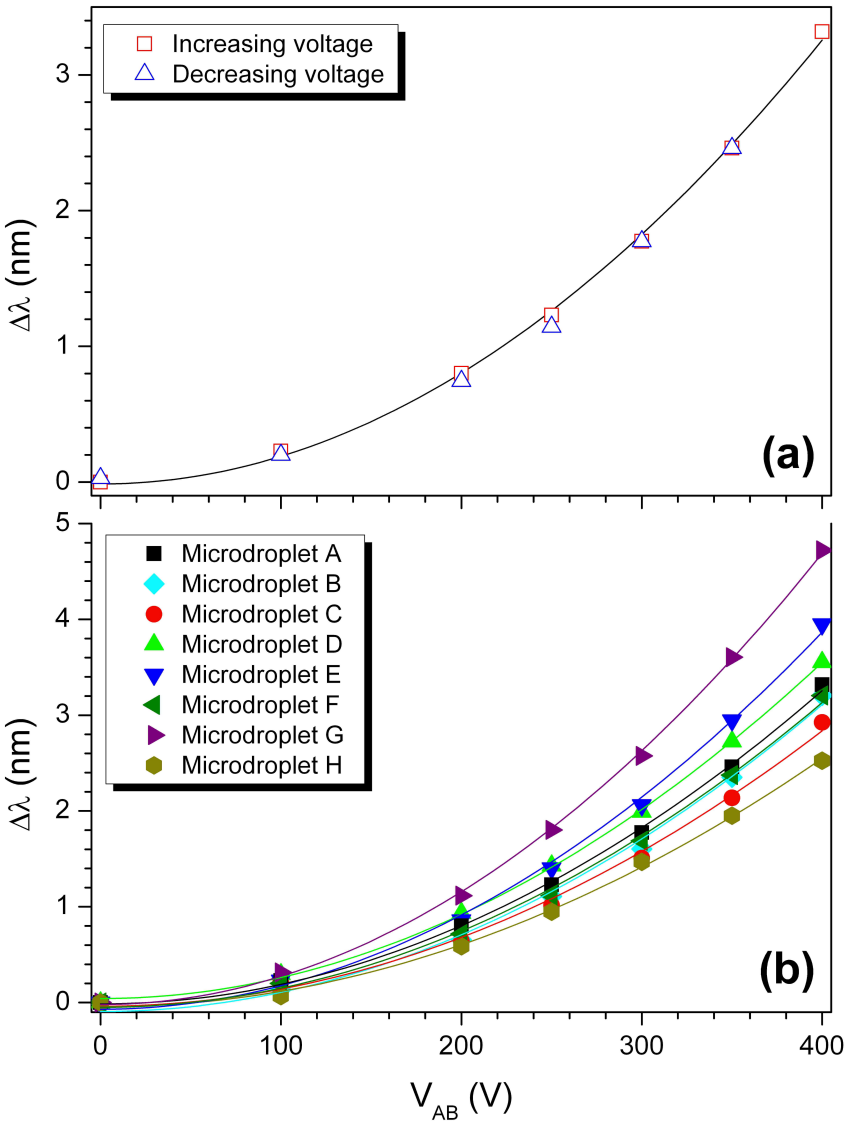


Figure 5.6: (a) Hysteresis curve of the spectral drift in the WGM A as a function of $V_{AB}$ as $V_{AB}$ is gradually increased from 0 to 400 V (squares) and decreased from 400 to 0 V (triangles). Solid line shows the parabolic best fit function to squares: $\Delta\lambda = 0.01453 + 2.04 \times 10^{-5} V_{AB}^2$. (b) Spectral drifts of the WGMs in eight different microdroplets including the microdroplet discussed in Fig. 5.4 as a function of increasing $V_{AB}$. Solid lines are the parabolic best fit functions. Diameters of microdroplets B, C, D, E, F, G, and H are 5, 6, 7.5, 7, 6.5, 7, and 6 $\mu$m respectively. A maximum spectral drift of 4.7 nm is observed at 400 V in microdroplet G.

The parabolic dependence between the spectral shift and $V_{AB}$ of the WGM A in Fig.5.6 is clearly observed in Fig.5.6a. The best fit function for experimental results is $\lambda = \lambda_0 + 2.04 \times 10^{-5} V_{AB}^2$. There is a slight difference between the experimental and theoretical best fit functions. Before we calculated the theoretical best fit function according to our electrowetting setup and we found that $\lambda = \lambda_0 + 1.53 \times 10^{-5} V_{AB}^2$. The reason of this slight difference is the variations of the unbiased contact angle from 150° . Also, the reversibility of the WGM A is demonstrated in Fig.5.6a. There is no hysteresis between the initial and final spectral positions of WGM A. Therefore the spectral tuning with electrowetting is reversible. Fig.5.6b shows the plots of spectral drift for eight microdroplets of the same chamber used in the experiment. The calculated parabolic coefficients for these microdroplets are between $1.56 \times 10^{-5}$ $mm/V^2$ for microdroplet H and $2.94 \times 10^{-5}$ $mm/V^2$ for microdroplet G. The observed spectral shifts are between 4.7 nm for microdroplet G and 2.3 nm for microdroplet H at 400 V. The variation of the unbiased contact angle causes the change in the parabolic coefficient. The estimated unbiased contact angles for microdroplet G and microdroplet H are 135° and 150°, respectively.

## *5.5 Summary*

Using electrowetting, we demonstrate reversible spectral tuning of the whispering gallery modes of glycerol/water microdroplets standing on a superhydrophobic surface by up to 4.7 nm at 400 V. Our results can inspire electrically tunable optical switches and filters based on microdroplets on a superhydrophobic surface. The sensitivity of the observed spectral drift to the contact angle can also be used to measure the contact angles of microdroplets on a superhydrophobic surface.

# Chapter 6

# CONCLUSION

This thesis has investigated spectral tuning of liquid microdroplets standing on a superhydrophobic surface by using a focused infrared laser or electrowetting. First, superhydrophobic surface preparation, experimental setup and microdroplet generation were explained. Then a lumped equation model was defined for the evaporation and growth of microdroplets due to the local heating by a focused infrared laser. Laser induced heating was obtain by calculating the absorption efficiency using the normalized approximation of generalized Lorentz-Mie theory. Glycerol-water and NaCl-water microdroplets were used in the experiments.

The spectral tuning of glycerol-water microdroplets standing on a superhydrophobic surface were examined by computationally and experimentally The tuning mechanism was based on the size change of the binary microdroplet controlled by focused infrared laser through evaporation and condensation of contents of the microdroplet owing to the laser-induced heating. The theoretical results were found to be in good qualitative agreement with the experimental measurements. Firstly, a scattering force calculation for a glycerol-water microdroplet was made to show that the optical scattering force could not be main reason of the observed large spectral tuning. The effects of chamber humidity, size of microdroplet and laser power on the tuning mechanism were examined. It was found that highly reversible large ($> 30$ nm) spectral tuning can be achieved using this technique. Large size changes were mainly caused by the evaporation of water content in the microdroplet. The spectral tuning was independent of the microdroplet size but it was very sensitive to the relative water humidity in the chamber. Since relative water humidity in the chamber increased, the spectral tuning sensitivity increased rapidly. The computational and experimental results indicated that irreversibility was mainly caused by evaporation of glycerol and reversibility could be increased dramatically when air in the chamber was saturated with glycerol vapor. Also, the reversibility increased with increasing the relative water humidity in the chamber.

Full reversible spectral tuning was obtained by using NaCl-water microdroplet standing on a superhydrophobic surface. The observed spectral tuning was larger than 40 nm. Also the computational results obtained by using the lumped system formulation model agreed with the experimental results. In addition to full reversible spectral tuning a self-stabilization mechanism was demonstrated for NaCl-water microdroplets that make their volume and WGM spectrum resilient to external perturbations Computations and experiments confirmed the explanation of the self-stabilization mechanism by the presence of WGM absorption resonances when scanning the power of an infrared laser focused at the rim of the microdroplet. A hsyteretic behavior was observed, if the infrared laser become resonant with a WGM absorption resonances within the photothermal tuning cycle. Self-stable equilibrium was observed on one side of the hysteresis loops, when the power was decreased. The self-stabilization mechanism provided a locking of the microdroplet size and spectrum for hours, since it relied on the water absorption at the infrared region and independent of the dye photobleaching. Spectral positions of the WGM were self-stabilized for several hours, corresponding to a radius stabilization of only a few nanometers. The WGM spectrum was also switched reversibly between the locked and unlocked states by using the bistable nature of the system.

Additionally, a reversible electric tuning mechanism to tune the WGMs of glycerol-water microdroplets by up to 4.7 nm at 400 V. This technique can be improved for future applications. For example the use of large microdroplets makes the spectral tuning independent from the value of the equatorial radius. In addition to that the high quality WGMs that circulates in the equatorial plane can be excited separately by using fiber coupling. As a final point, the spectral tuning with electrowetting can be used to measure precisely the contact angles of the microdroplets because there is a strong dependence between the unbiased contact angle and the parabolic coefficient.

# APPENDIX A

## Mathematica Program for Calculation of Modified Absorption Efficiency ($\tilde{Q}_{abs}$)

```
Off[General::spell1]
changealphaby = "r";
(*resn=1.3837+1.4361*10^-6*I;*)
resn = 1.33 + 1.20232 * 10 ^ -6 * I;

lambda = 1064 * 10 ^ -9;   (*in meters*)
c = 2.99792458 * 10 ^ 8;   (*in meters/second*)
mu0 = 1.25663706 * 10 ^ -6; (*in m.kg.s^-2. A^-2;*)
alphamin = 20.66837;  alphamax = 26.57362;
(*range of alpha values for Q vs alpha plot*)
resradius = alphamin * lambda / (2 * Pi);  (*in meters. Corresponds to alpha=66.13879*)

w0 = 1000 * 10 ^ -9;



ndp = 2001; (*# of data points in the graph*)
xx0 = 4 * 10 ^ -6; ; yy0 = 0;  zz0 = 0;  (*Focus coordinates*)
(************DEFYNING PSI AND ZHETA NECESSARY FOR al AND bl**************)
psil[l_, x_] = Sqrt[Pi * x / 2] * BesselJ[l + 0.5, x];
ksil[l_, x_] = -Sqrt[Pi * x / 2] * BesselY[l + 0.5, x];
zhetaL[l_, x_] = psil[l, x] - I * ksil[l, x];
psiprimeL[l_, x_] = D[psil[l, x], x];
 zhetaprimeL[l_, x_] = D[zhetaL[l, x], x];
(*%%%%%%%%%%%%%%%%%%%%%%%%%%%%%%%%%%%%%%%%%%%%%%%%%%%%%*)
pbeam = {}; pscatt = {}; cext = {}; csca = {}; iIinc = {};
cabs = {}; pabs = {}; qQabstilda = {}; xalpha = {};
(*%%%%%%%%%%%%%%%%%%%%%%%%%%%%%%%%%%%%%%%%%%%%%%%%%%%%%*)
For[abc = 1, abc ≤ ndp, abc = abc + 1,
  x0 = alphamin + (alphamax - alphamin) * (abc - 1) / (ndp - 1);
  lmax = Round[x0 + 4.3 * x0 ^ (1 / 3) + 2];
  (*%%%%%%%%%%%%%%%%%%%%%%%%%%%%%%%%%%%%%%%%%%%%%%%%%%%%%*)
  If[ changealphaby == "r", {kext = 2 * Pi / lambda; resradius = x0 / kext; dummy = 1},
   {kext = x0 / resradius; w0 = w0overlambda * (2 * Pi / kext);} ];
  (*%%%%%%%%%%%%%%%%%%%%%%%%%%%%%%%%%%%%%%%%%%%%%%%%%%%%%*)
  eE0 = 1;

  addedbeamL = 0;  addedscaL = 0; addedCextL = 0; addedCscaL = 0;
  For[lL = 1, lL ≤ lmax, lL = lL + 1,
   p1 = psil[lL, x0]; p2 = psil[lL, resn * x0]; p3 = psiprimeL[lL, x0];
   p4 = psiprimeL[lL, resn * x0]; p5 = zhetaL[lL, x0]; p6 = zhetaprimeL[lL, x0];
   al = -(p4 * p1 - resn * p2 * p3) / (resn * p2 * p6 - p4 * p5);
   bl = -(resn * p4 * p1 - p2 * p3) / (p2 * p6 - resn * p4 * p5);

   s = 1 / (kext * w0);  dD = (1 - (2 * I * s * zz0) / w0) ^ -1;
   fFl = dD * Exp[-dD * xx0 ^ 2 / w0 ^ 2] * Exp[-dD * s ^ 2 * (lL + 0.5) ^ 2];
   rfpls = xx0 / Sqrt[xx0 ^ 2];  rfmns = xx0 / Sqrt[xx0 ^ 2];
   pP = -(lL + 0.5) * Sqrt[xx0 ^ 2 / w0 ^ 2] * (2 * s / I); qQ = -I * pP;

   If[ lL > mMthreshold, mMmax = mMthreshold, mMmax = lL];

   addedbeamM = 0; addedscaM = 0; addedCextM = 0; addedCscaM = 0;
   For[mM = -mMmax, mM ≤ -1, mM = mM + 1,
    aAlm = fFl * ((-rfpls / (lL + 0.5)) ^ (Abs[mM] - 1)) *
      (BesselJ[Abs[mM] - 1, pP] - (rfpls^2) * BesselJ[Abs[mM] + 1, pP]);
```

```
bBlm = (-fFl / I) * ((-rfpls / (lL + 0.5)) ^ (Abs[mM] - 1)) *
          (BesselJ[Abs[mM] - 1, pP] + (rfpls ^ 2) * BesselJ[Abs[mM] + 1, pP]);
       factcoeff = Factorial[lL + Abs[mM]] / Factorial[lL - Abs[mM]];
       addedbeamM = addedbeamM + factcoeff * (Abs[aAlm] ^ 2 + Abs[bBlm] ^ 2);
       addedscaM =
         addedscaM + factcoeff * (Abs[aAlm] ^ 2 * Abs[al] ^ 2 + Abs[bBlm] ^ 2 * Abs[bl] ^ 2);
       addedCextM = addedCextM + factcoeff * (al * Abs[aAlm] ^ 2 + bl * Abs[bBlm] ^ 2);
       addedCscaM = addedscaM;
       ];
     mM = 0;
     aAlm =
       fFl * (2 * lL * (lL + 1) / (lL + 0.5)) * (xx0 / Sqrt[xx0 ^ 2 + yy0 ^ 2]) * BesselJ[1, pP];
     bBlm = (aAlm / xx0) * yy0;
     factcoeff = 1;
     addedbeamM = addedbeamM + factcoeff * (Abs[aAlm] ^ 2 + Abs[bBlm] ^ 2);
     addedscaM =
       addedscaM + factcoeff * (Abs[aAlm] ^ 2 * Abs[al] ^ 2 + Abs[bBlm] ^ 2 * Abs[bl] ^ 2);
     addedCextM = addedCextM + factcoeff * (al * Abs[aAlm] ^ 2 + bl * Abs[bBlm] ^ 2);
     addedCscaM = addedscaM;

     For[mM = 1, mM ≤ mMmax, mM = mM + 1,
       aAlm = fFl * ((-rfmns / (lL + 0.5)) ^ (mM - 1)) *
         (BesselJ[mM - 1, pP] - (rfmns ^ 2) * BesselJ[mM + 1, pP]);
       bBlm = (fFl / I) * ((-rfmns / (lL + 0.5)) ^ (mM - 1)) *
         (BesselJ[mM - 1, pP] + (rfmns ^ 2) * BesselJ[mM + 1, pP]);
       factcoeff = Factorial[lL + Abs[mM]] / Factorial[lL - Abs[mM]];
       addedbeamM = addedbeamM + factcoeff * (Abs[aAlm] ^ 2 + Abs[bBlm] ^ 2);
       addedscaM =
        addedscaM + factcoeff * (Abs[aAlm] ^ 2 * Abs[al] ^ 2 + Abs[bBlm] ^ 2 * Abs[bl] ^ 2);
       addedCextM = addedCextM + factcoeff * (al * Abs[aAlm] ^ 2 + bl * Abs[bBlm] ^ 2);
       addedCscaM = addedscaM;
      ];
     addedbeamL = addedbeamL + ((2 * lL + 1) / (lL * (lL + 1))) * addedbeamM;
     addedscaL = addedscaL + ((2 * lL + 1) / (lL * (lL + 1))) * addedscaM;
     addedCextL = addedCextL + ((2 * lL + 1) / (lL * (lL + 1))) * addedCextM;
     addedCscaL = addedscaL;
     ];
   pbeam = Append[pbeam, (eE0 ^ 2 / (2 * mu0 * c)) * (Pi / (4 * kext ^ 2)) * addedbeamL];
   pscatt = Append[pscatt, (eE0 ^ 2 / (2 * mu0 * c)) * (Pi / (kext ^ 2)) * addedscaL];
   cext = Append[cext, (lambda ^ 2 / Pi) * Re[addedCextL]];
   csca = Append[csca, (lambda ^ 2 / Pi) * addedCscaL];
   iIinc = Append[iIinc, Part[pscatt, abc] / Part[csca, abc]];
   cabs = Append[cabs, Part[cext, abc] - Part[csca, abc]];
   pabs = Append[pabs, Part[iIinc, abc] * Part[cabs, abc]];
   qQabstilda = Append[qQabstilda, Part[pabs, abc] / Part[pbeam, abc]];
   xalpha = Append[xalpha, x0]; Print[abc];
  ];
Put[qQabstilda, " q16 "] (expr >> filename)
Put[xalpha, " alpha16 "] (expr >> filename)
ListPlot[qQabstilda];
```

# VITA

Yasin Karadağ was born in Istanbul, Turkey on November 1, 1983. He received his B. Sc. degree in physics from Bilkent University, Ankara, Turkey, in 2007. He joined the M. Sc. program in Physics at Koç University in 2007. He received his M. Sc. degree from Koç University in 2009. His master thesis work was titled as *Spectral Tuning of Liquid Microdroplets Standing on a Superhydrophobic Surface by Using a Focused Infrared Laser or Electrowetting*. He will start his Ph.D degree at Koç University. He is a student member of International Society for Optical Engineering (SPIE) and Optical Society of America (OSA).

## LIST OF PUBLICATIONS

1. A. Kiraz, S. Ç. Yavuz, Y. Karadağ, A. Kurt, A. Sennaroglu, and H. Çankaya. "Large spectral tuning of liquid microdroplets standing on a superhydrophobic surface using optical scattering force" Appl. Phys. Lett. 91, 231102 (2007)

2. A. Kiraz, Y. Karadağ, and A. F. Coskun. "Spectral tuning of liquid microdroplets standing on a superhydrophobic surface using electrowetting" Appl. Phys. Lett. 92, 191104 (2008)

3. A. Kiraz, Y. Karadağ, and M. Muradoğlu. "Large spectral tuning of a water-glycerol microdroplet by a focused laser: characterization and modeling" Phys. Chem. Chem. Phys. 10, 6446-6454 (2008)

4. A. Kiraz, Y. Karadag, S. C. Yorulmaz, and M. Muradoglu. "Reversible photothermal tuning of a salty water microdroplet" Phys. Chem. Chem. Phys. 11, 2597-2600 (2009)

5. Y. Karadag, M. Mestre, and A. Kiraz. "Photothermal self-stability and optical bistability of single NaCl-water microdroplets on a superhydrophobic surface" Phys. Chem. Chem. Phys. 11, 7145-7151 (2009)

# BIBLIOGRAPHY

[1] K. J. Vahala, "Optical microcavities," *Nature*, vol. 424, p. 839, 2003.

[2] V. S. Ilchenko and A. B. Matsko, "Optical resonators with whispering-gallery modes-part ii: Applications," *IEEE J. Sel. Topics Quantum Electron.*, vol. 12, pp. 15–31, 2006.

[3] V. L. Seguin, "Whispering-gallery mode lasers with doped silica microspheres," *Optical Materials*, vol. 11, pp. 153–165, 1999.

[4] A. Kiraz, A. Kurt, M. A. Dündar, and A. L. Demirel, "Simple largely tunable optical microcavity," *Appl. Phys. Lett.*, vol. 89, p. 081118, 2006.

[5] D. K. Armani, T. J. Kippenberg, S. M. Spillane, and K. J. Vahala, "Ultra-high-Q toroid microcavity on a chip," *Nature*, vol. 421, pp. 925–928, 2003.

[6] H. Mabucci, Q. A. Turchette, M. S. Chapman, and H. J. Kimble, "Real-time detection of individual atoms falling through a high-finesse optical cavity," *Opt. Lett.*, vol. 21, p. 1393, 1996.

[7] G. Rempe, "One-atom in an optical cavity-spatial-resolution beyond the standard diffraction limit," *Appl. Phys.*, vol. 60, pp. 233–237, 1995.

[8] C. J. Hood, T. W. Lynn, A. C. Doherty, A. S. Parkins, and H. J. Kimble, "The atom-cavity microscope: Single atoms bound in orbit by single photons," *Science*, vol. 287, p. 14471453, 2000.

[9] P. W. H. Pinkse, T. Fischer, P. Maunz, and G. Rempe, "Trapping an atom with single photons," *Nature*, vol. 404, pp. 365–368, 2000.

[10] Y. Shimizu, "Control of light pulse propagation with only a few cold atoms in a high-finesse microcavity," *Phys. Rev. Lett.*, vol. 89, p. 233001, 2002.

[11] S. Suzuki, Y. Hatakeyama, Y. Kokubun, and S. T. Chu, "Precise control of wavelength channel spacing of microring resonator add-drop filter array," *J. Lightwave Technol.*, vol. 20, p. 745750, 2002.

[12] K. Djordjev, S. J. Choi, and P. D. Dapkus, "Microdisk tunable resonant filters and switches," *IEEE Phot. Technol. Lett.*, vol. 14, p. 828830, 2002.

[13] P. Rabiei, W. H. Steier, C. Zhang, and L. R. Dalton, "Polymer micro-ring filters and modulators," *J. Lightwave Technol.*, vol. 20, p. 19681975, 2002.

[14] F. Vollmer, D. Braun, A. Libchaber, M. Khoshsima, I. Teraoka, and S. Arnold, "Polymer micro-ring filters and modulators," *Appl. Phys. Lett.*, vol. 80, p. 4057, 2002.

[15] M. A. Dundar, "Inducing a novel optical microcavity: A glycerol/water microdroplet on a superhydrophobic surface," Master's thesis, Koc Universty, 2007.

[16] A. Checco, P. Guenoun, and J. Daillant, "Nonlinear dependence of the contact angle of nanodroplets on contact line curvature," *Phys. Rev. Lett.*, vol. 91, p. 186101, 2003.

[17] H. Azzouz, "Liquid droplet dye laser," Master's thesis, Technical Universty of Denmark, 2005.

[18] V. Lefevre-Seguin, J. C. Knight, V. Sandogdar, D. S. Weiss, J. Hare, J. M. Raimond, and S. Haroche, "Very high Q whispering-gallery modes in silica microspheres for cavity-QED experiments," in *Optical Processes in Microcavities* (R. K. Chang and A. J. Campillo, eds.), vol. 3, pp. 101–133, World Scientific, 1996.

[19] M. H. Fields, J. Popp, and R. K. Chang, "Nonlinear optics in microspheres," in *Progress in Optics* (E. Wolf, ed.), vol. 41, pp. 1–95, Elsevier, 2000.

[20] G. Grehan, B. Maheu, and G. Gouesbet, "Scattering of laser beams by mie scatter centers: numerical results using a localized approximation," *Appl. Opt.*, vol. 25, pp. 3539–3548, 1986.

[21] J. A. Lock, "Improved gaussian beam-scattering algorithm," *Appl. Opt.*, vol. 34, pp. 559–570, 1995.

[22] J. A. Lock, "Excitation efficiency of a morphology-dependent resonance by a focused gaussian beam," *J. Opt. Soc. Am. A*, vol. 15, pp. 2986–2994, 1998.

[23] A. K. Ray, R. D. Johnson, and A. Souyri, "Dynamic behavior of single glycerol droplets in humid air streams," *Langmuir*, vol. 5, pp. 133–140, 1989.

[24] H. Tu and A. K. Ray, "Measurement of activity coefficients from unsteady state evaporation and growth of microdroplets," *Chem. Eng. Comm.*, vol. 192, pp. 474–498, 2005.

[25] R. G. Picknett and R. J. Bexon, "The evaporation of sessile or pendant drops in still air," *J. Colloid Interface Sci.*, vol. 79, pp. 667–677, 1977.

[26] G. McHale, S. Aqil, N. J. Shirtcliffe, M. I. Newton, and H. Y. Erbil, "Analysis of droplet evaporation on a superhydrophobic surface," *Langmuir*, vol. 21, pp. 11053–11060, 2005.

[27] H. Tu, *Application of Light Scattering in Studies of Transport, Thermodynamics, Light Absorption, and Electric Properties of Single Droplets*. PhD thesis, University of Kentucky, 2001.

[28] D. R. Lide, *CRC Handbook of Chemistry and Physics, Internet Version 2005, <http://www.hbcnetbase.com>*. CRC Press, 2005.

[29] S.-X. Qian, J. B. Snow, H. M. Tzeng, and R. K. Chang, "Lasing droplets: Highlighting the liquid-air interface by laser emission," *Science*, vol. 231, p. 486, 1986.

[30] V. V. Datsyuk, "Optics of microdroplets," *J. Mol. Liq.*, vol. 84, pp. 1308–1316, 2001.

[31] I. N. Tang, A. C. Tridico, and K. H. Fung, "Thermodynamic and optical properties of sea salt aerosols," *J. Geophys. Res.*, vol. 102, pp. 23269–23275, 1997.

[32] D. Segelstein, "The complex refractive index of water," Master's thesis, University of Missouri, Kansas City, 1981.

[33] E. J. G. Peterman, F. Gittes, and C. F. Schmidt, "Laser-induced heating in optical traps," *Biophys. J.*, vol. 84, pp. 1308–1316, 2003.

[34] G. Gouesbet and J. A. Lock, "Rigorous justification of the localized approximation to the beam-shape coefficients in generalized lorenz-mie theory. ii. off-axis beams," *J. Opt. Soc. Am. A*, vol. 11, pp. 2516–2525, 1994.

[35] J. P. Barton, D. R. Alexander, and S. A. Schaub, "Internal and near-surface electromagnetic fields for a spherical particle irradiated by a focused laser beam," *J. Appl. Phys.*, vol. 64, pp. 1632–1639, 1988.

[36] J. P. Barton, D. R. Alexander, and S. A. Schaub, "Internal fields of a spherical particle illuminated by a tightly focused laser beam: Focal point positioning effects at resonance," *J. Appl. Phys.*, vol. 65, pp. 2900–2906, 1989.

[37] C. F. Bohren and D. R. Huffman, *Absorption and Scattering of Light by Small Particles.* Wiley-VCH, 1998.

[38] A. Ashkin, "Forces of a single-beam gradient laser trap on a dielectric sphere in the ray optics regime," *Biophys. J.*, vol. 61, pp. 569–582, 1992.

[39] A. Kiraz, S. Ç. Yavuz, Y. Karadağ, A. Kurt, A. Sennaroglu, and H. Çankaya, "Large spectral tuning of liquid microdroplets standing on a superhydrophobic surface using optical scattering force," *Appl. Phys. Lett.*, vol. 91, p. 231102, 2007.

[40] J. P. Reid, H. Meresman, L. Mitchem, and R. Symes, "Spectroscopic studies of the size and composition of single aerosol droplets," *Int. Rev. Phys. Chem.*, vol. 26, pp. 139–192, 2007.

[41] S. Arnold, K. M. Leung, and A. Pluchino, "Optical bistability of an aerosol particle," *Opt. Lett.*, vol. 11, pp. 800–802, 1986.

[42] S. Arnold, T. R. O'Keeffe, K. M. Leung, L. M. Folan, T. Scalese, and A. Pluchino, "Optical bistability of an aqueous aerosol particle detected through light scattering: theory and experiment," *Appl. Opt.*, vol. 29, pp. 3473–3478, 1990.

[43] A. Kiraz, A. Kurt, M. A. Dündar, M. Y. Yüce, and A. L. Demirel, "Volume stabilization of single, dye-doped water microdroplets with femtoliter resolution," *J. Opt. Soc. Am. B*, vol. 24, pp. 1824–1828, 2007.

[44] J. A. Lock and G. Gouesbet, "Rigorous justification of the localized approximation to the beam-shape coefficients in generalized lorenz-mie theory. i. on-axis beams," *J. Opt. Soc. Am. A*, vol. 11, pp. 2503–2515, 1994.

[45] A. Serpengüzel, J. C. Swindal, R. K. Chang, and W. P. Acker, "Two-dimensional imaging of sprays with fluorescence, lasing, and stimulated raman scattering," *Appl. Opt.*, vol. 31, pp. 3543–3551, 1992.

[46] F. Mugele and J. C. Baret, "Electrowetting: from basics to applications," *J. Phys: Condens. Matter*, vol. 17, pp. 705–774, 2005.

[47] G. Chen, M. M. Mazumder, Y. R. Chemla, A. Serpengüzel, R. K. Chang, and S. C. Hill, "Wavelength variation of laser emission along the entire rim of slightly deformed microdroplets," *Opt. Lett.*, vol. 18, pp. 1993–1995, 1993.